Journal of Materials Chemistry A

REVIEW

View Article Online
View Journal | View Issue

Published on 20 June 2017. Downloaded by University of Western Ontario on 27/07/2017 20:28:34.

Check for updates

Cite this: J. Mater. Chem. A, 2017, 5, 13882

Carbon nanofiber-based nanostructures for lithium-ion and sodium-ion batteries

Weihan Li,[ab] Minsi Li,[b] Keegan R. Adair,[b] Xueliang Sun *[b] and Yan Yu *[ac]

Carbon nanofibers (CNFs) belong to a class of one-dimensional (1D) carbonaceous materials with excellent electronic conductivity, leading to their use as conductive additives in electrode materials for lithium-ion batteries (LIBs) and sodium-ion batteries (NIBs). Additionally, CNFs show excellent lithium- and sodium-storage performance when used directly as anode materials *via* template and activation strategies to produce numerous intercalation sites. In the case of the non-carbon electrodes for LIBs & NIBs, CNFs are capable of functioning as electron conducting and porous substrates to enhance the overall electronic & ionic conductivity and stabilizing the structures of electrodes during cycling, facilitating the improvement of the electrochemical performance of non-carbon anode and cathode materials. In this review, we present a comprehensive summary of the recent progress of CNF application in LIBs and NIBs, focusing on the structural evolution and the resulting improvements in electrochemical performance and demonstrating the importance of advancements in CNF-based electrode materials.

Received 10th March 2017
Accepted 20th June 2017

DOI: 10.1039/c7ta02153d

rsc.li/materials-a

1. Introduction

Recently, renewable energy technology has been intensively studied to address the problems arising from the exploitation of fossil fuels and their serious environmental impacts. The emission of large amounts of carbon dioxide from the burning of fossil fuels enhances radiative forcing and contributes significantly to global warming, leading to major adverse effects on the environment.[1–4] To mitigate the negative effects of a fossil-based economy, sources of renewable energy are required to reduce the dependence on fossil fuels and emission of greenhouse gases.[5,6] The primary strategy for the utilization of renewable energy sources, such as wind and solar power, is to generate electrical energy. However, the practical application of these renewable energy technologies is hindered by the intermittent characteristic. In this regard, it's crucial to develop energy storage systems capable of storing the harvested electrical energy.[7] Among modern energy storage technologies, secondary batteries have become one of the most prominent and fast-growing systems due to the efficient storage and

[a]Key Laboratory of Materials for Energy Conversion, Chinese Academy of Sciences, Department of Materials Science and Engineering, University of Science and Technology of China, Hefei, Anhui 230026, P. R. China. E-mail: yanyumse@ustc.edu.cn; Tel: +86-551-63607179

[b]Department of Engineering, The University of Western Ontario, London, Ontario, Canada. E-mail: xsun@eng.uwo.ca; Tel: +1-519-661-2111 ext. 87759

[c]State Key Laboratory of Fire Science, University of Science and Technology of China, Hefei, Anhui, 230026, P. R. China

Weihan Li completed his doctorate in Material Sciences under the supervision of Prof. Yan Yu at the University of Science and Technology of China, Hefei, in 2016. He is currently a postdoctoral fellow in Prof. Xueliang (Andy) Sun's Nanomaterials and Energy Group at the University of Western Ontario, Canada. His research interests mainly include synthesis and application of nanomaterials for lithium-ion batteries and sodium-ion batteries.

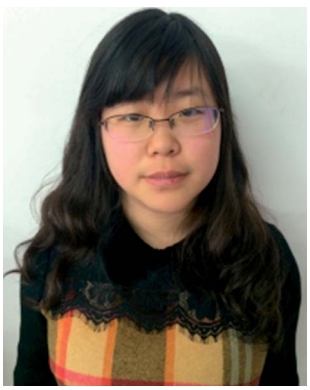

Minsi Li received the B.S. degree from the University of Science and Technology of China, Hefei, Anhui, P. R. China in 2016. She is currently a Ph.D. candidate in Prof. Xueliang (Andy) Sun's Nanomaterials and Energy Group at the University of Western Ontario, Canada. Her research interests mainly include preparation and characterization of nanomaterials for sodium-ion batteries.

This journal is © The Royal Society of Chemistry 2017

Published on 20 June 2017. Downloaded by University of Western Ontario on 27/07/2017 20:28:34.

delivery of electrical energy. In recent times, lithium-ion batteries (LIBs) have been widely used in portable electronics and electric vehicles, owing to the high energy-conversion efficiency, long working life and environmental benignity.[8–12] In addition, as an alternative battery technology, sodium-ion batteries have attracted great attention due to the abundance and low cost of sodium resources and hold great potential for applications in large-scale grid energy storage.[13–16]

Considering the increasing demand for higher energy and power density devices with longer working lifetimes, significant efforts have been devoted to the research of LIBs and NIBs to improve electrochemical performance. The electrochemical performance of LIBs and NIBs, including energy density, operation current densities, and working life time, is mainly determined by the electrode materials.[17,18] State-of-the-art LIBs often employ the use of metal oxides or phosphate materials (*e.g.* $LiCoO_2$, $LiNiCoAlO_2$ and $LiFePO_4$) and graphite-based materials as the cathodes and anodes, respectively. Similarly, the current research of NIBs focuses on the development of advanced electrode materials, such as carbon-based anodes and phosphate-based cathodes to promote the industrialization of the NIBs.[19–21] In the case of electrode materials, electronic and ionic conductivities are two crucial factors presenting enormous influence on the electrochemical performance, which are usually modified through doping,[22–25] control of material size,[26–29] and introduction of conductive substrates or additives (*e.g.* conductive metal, polymers and carbon-based materials).[30–35] Among these conductive additives, many carbon-based materials have been widely applied, including graphene (rGO),[36–39] carbon nanotubes (CNTs),[40–43] and carbon nanofibers (CNFs),[44–47] due to their good electronic conductivity and compatibility with other electrode materials. In the meantime, carbon-based materials can be also directly utilized as anode materials for LIBs and NIBs.[23,48–50]

With a novel one-dimensional (1D) carbon structure, CNFs present good access to electrolytes and high electronic conductivity along longitudinal directions. In this regard, various studies have reported the application of carbon nanofibers in LIBs and NIBs and showed highly improved lithium- & sodium-storage performance, indicating the high research significance of carbon nanofibers for LIBs and NIBs.[23,44,50,51] In this review, we focus on the application of CNFs in LIBs and NIBs by summarizing the preparation strategies, structures and composition of CNF-based electrodes in relation to the electrochemical performance.

Keegan Adair received his B.Sc. in chemistry from the University of British Columbia in 2016. He is currently a Ph.D. candidate in Prof. Xueliang (Andy) Sun's Nanomaterials and Energy Group at the University of Western Ontario, Canada. His research interests include the design of nanomaterials for lithium-ion batteries and nanoscale interfacial coatings for battery applications.

Xueliang (Andy) Sun is a Canada Research Chair in Development of Nanomaterials for Clean Energy, a fellow of the Royal Society of Canada and Canadian Academy of Engineering and a full professor at the University of Western Ontario, Canada. Dr Sun received his PhD in Materials Chemistry in 1999 at the University of Manchester, UK, which he followed up by working as a postdoctoral fellow at the University of British Columbia, Canada, and as a Research Associate at L'Institut National de la Recherche Scientifique (INRS), Canada. His current research interests are associated with advanced materials for electrochemical energy storage and conversion, including electrocatalysis in fuel cells and electrodes in lithium-ion batteries and metal–air batteries.

2. Carbon nanofibers and preparation strategies

Carbon nanofibers are one-dimensional sp^2-hybridized carbon nanostructures consisting of discontinuous filaments with aspect ratios (length/diameter) greater than 100. CNFs differ from carbon nanotubes which have structures like wrapping graphene layers to form perfect cylinders.[52,53] Various strategies have been applied to prepare CNFs, including the catalytic chemical vapor deposition growth, electrospinning, template-based synthesis and biomass methods.[16,54–59]

2.1 Chemical vapor deposition growth

The chemical vapor deposition growth of CNFs is usually conducted with metal catalysts, and gaseous hydrocarbon

Yan Yu is a Professor of Material Science in University of Science and Technology of China (USTC). She received her Ph.D. in Material Science at USTC in 2006. From 2007 to 2008, she worked as a postdoctoral fellow at Florida International University. After that she received a Humboldt Research Fellowship from the Alexander von Humboldt Foundation and worked at the Max Planck Institute for Solid State Research in Stuttgart, Germany. Her current research interests mainly include design of novel nanomaterials for clean energy, especially for batteries, and the fundamental science of energy storage systems.

Published on 20 June 2017. Downloaded by University of Western Ontario on 27/07/2017 20:28:34.

precursors under high temperature.[60] During the process, gaseous hydrocarbons act as the carbon source (*e.g.* methane, acetylene, hexane and ethylene) and decompose in the temperature range of 700 to 1200 K. Metal nanoparticle catalysts composed of iron, nickel, cobalt and various alloys, are capable of dissolving carbon and/or forming metal carbides at the surface, the formed carbon atoms at the surface of catalytic metals would dissolve in the metal and diffuse through the metals. After continuous decomposition of gaseous hydrocarbon and diffusion through the bulk metals, carbon atoms precipitate at the other side of metals and form graphitic structures, completing the preparation of vapor grown CNFs (VGCNFs). During the growth process, the morphology of the metal nanoparticle catalysts is one crucial factor in determining the structures of VGCNFs. Two types of VGCNFs have been fabricated *via* different metal nanoparticles, namely cup-stacked CNFs and the platelet-stacked CNFs.[61–64] As shown in Fig. 1A and B, Pt nanocrystals and Fe nanoflakes are applied as catalysts to prepare stacked CNFs and platelet-stacked CNFs, respectively.

2.2 Electrospun carbon nanofibers

In addition to VGCNFs, numerous kinds of electrospun 1D polymer nanofibers have been utilized as precursors to form carbon nanofibers through carbonization, which have been widely applied in LIBs and NIBs. The electrospinning process is a fast and efficient strategy to fabricate 1D polymer nanofibers and has obtained intensive research attention in the design and fabrication of nanostructured electrodes.[16,65,66] Fig. 1C shows the typical process of the electrospinning technology. Through the use of a syringe pump, the polymer solution in the syringe forms a droplet at the tip of the metal needle owing to the surface tension. When a high voltage is applied between the metal needle and the collector, the droplet becomes elongated and forms a conical Taylor cone as a result of the electrostatic repulsive force at the surface.[67] When the voltage reaches a critical value, the electrostatic repulsive force overcomes the surface tension, leading to a liquid jet ejecting from the droplet and a continuous elongation of the stream due to the existing surface charge of the jet. The elongation process leads to the dramatic decrease of the diameter of the jet to hundreds or tens of nanometers.[16,68] Electrospinning is one facile technology utilized to fabricate polymer nanofibers, with numerous polymer precursors commonly employed to form nanofibers, including poly(vinyl alcohol) (PVA), polyacrylonitrile (PAN), poly(vinylpyrrolidone) (PVP), and poly(ethylene oxide) (PEO).[16] Through carbonization of the polymer nanofibers in an inert atmosphere, CNFs can be prepared with the structures modified by tuning the precursor solutions and electrospinning parameters.[54,66] Additionally, composite nanofibers consisting of carbon and other LIB/NIB-electrochemically active materials have been fabricated *via* electrospinning through the introduction of active materials' precursors into the electrospinning precursor solutions or combining the active materials into the electrospun carbon nanofibers *via* other growth strategies, such as C–Sn nanofibers, C–Ge nanofibers, C–MoS_2 nanofibers and C–$Na_3V_2(PO_4)_3$ nanofibers.[45,47,69,70]

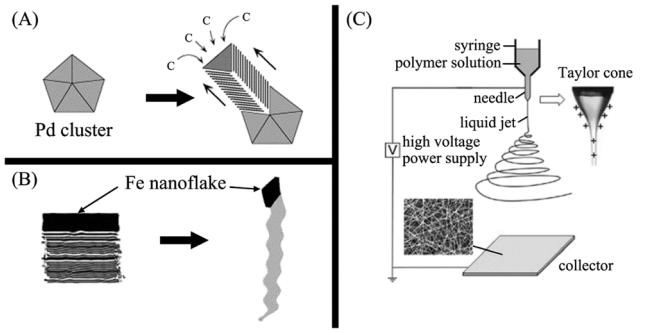

Fig. 1 Schematic illustration of the growth mechanism of (A) cup-stacked and (B) platelet-stacked vapor grown carbon nanofibers and (C) a fundamental electrospinning setup. Part (A), Reproduced with permission,[63] Copyright© 2001 Elsevier; Part (B), Reproduced with permission,[62] Copyright© 2005 Elsevier; Part (C), Reproduced with permission,[65] Copyright© 2004 Wiley.

2.3 Template-based strategies

In addition to the electrospinning technology, template-based strategies have been widely studied to fabricate polymer nanofibers. CNFs developed by a template-based synthesis often follow two synthetic routes: one popular route is CNFs based on hard-templates, while another is the solution-based synthesis of 1D polymer nanofibers *via* a template assembly route followed by carbonization.[71,72] In the case of the first route, anodic aluminum oxide (AAO) templates have been extensively applied to fabricate CNF arrays or hollow CNF arrays *via* chemical vapor deposition.[72,73] Previous studies have realized the preparation of hollow carbon nanofibers to encapsulate the pre-synthesized active material, such as Si–SiO_2 nanofibers.[74] On the other hand, the solution-based template assembly route is another method to prepare polymer nanofibers as precursors to CNFs. In 2010, Liu and co-workers[71] reported a general oxidative template assembly route to synthesize conducting polymer (*i.e.* polyaniline (PANI), polypyrrole (PPy), and poly(3,4-ethylenedioxythiophene) (PEDOT)) nanoclips, resulting from the orchestration of an insoluble complex. The insoluble complex is formed between an anionic oxidant ($S_2O_8^{2-}$) and a cationic surfactant. Based on this oxidative template assembly route, several studies have fabricated conducting polymer nanofibers, mainly PPy, which were then carbonized under an inert atmosphere to develop CNFs and for LIB & NIB applications.[48,75] Similar to the oxidative template assembly route, the self-assembly strategy is another way to get polymer nanofibers. Cao *et al.*[49] realized the preparation of hollow CNF anode materials for NIBs through carbonization of hollow PANI nanofibers, which were prepared *via* a self-assembly synthesis.

2.4 Biomass methods

In addition to the chemical synthesis strategies, biomass can be utilized in the fabrication process of CNFs. The main route of development of CNFs based on biomass methods is the carbonization of organic polymer nanofibers, such as bacterial cellulose, which have been directly utilized as anode materials

 This journal is © The Royal Society of Chemistry 2017

Published on 20 June 2017. Downloaded by University of Western Ontario on 27/07/2017 20:28:34.

or act as substrates to support other non-carbon anode or cathode materials for LIBs & NIBs.[76–78] Bacterial cellulose is an organic compound (*i.e.* $(C_6H_{10}O_5)_n$) with a nanofiber network produced by the bacteria.[79] After carbonization, the bacterial cellulose forms a CNF network, with improved electronic conductivity and pore access for electrolytes, indicating superior performance for application in LIBs & NIBs.

As displayed in Table 1, the carbon nanofibers prepared *via* the four strategies present a similar diameter range from 50 to 100 nm.[54,80–86] In addition, the chemical vapor deposition growth and template-based strategies can extend the diameter to 200 nm and carbon nanofibers with a diameter of more than 200 nm can be fabricated *via* electrospinning. Considering the limitation of preparation parameters (*e.g.* the growth time of VGCNFs, the scale of templates and precursors of the template-based and biomass strategies, respectively), the length of CNFs fabricated *via* the three strategies is limited to several to tens of micrometers. As the electrospinning is one continuous spinning strategies, the length of polymer nanofibers can be several centimeters, determining the same length of electrospun carbon nanofibers. In the case of electrical conductivity, related to the crystallization states of CNFs, the VGCNFs show the highest value, around 1×10^3 to 1×10^4 S cm^{-1}. For the other three strategies, the electrical conductivity of prepared CNFs is determined by the preparation parameters, including treatment temperature, heteroatom-doping content and precursors. In general, CNFs prepared through the four strategies can improve the overall electrical conductivity and finally the electrochemical performance of electrode materials when applied in batteries. In addition to the physical properties of CNFs, the cost of CNFs should be also considered in preparation of electrode materials for practical applications. The chemical vapor deposition growth strategy displays the highest cost, due to the low growth rate and high price of catalysts and precursor gas. In contrast, the commercial large-scale production low price of biomass precursors leads to the lower cost of the biomass strategy. And the cost of electrospinning and template-based strategies depends on the polymers and templates used in the strategies. It is ideal to balance the morphology & electrical conductivity and cost of CNFs to realize practical applications of CNF-based electrode materials.

3. Carbon nanofibers applied in lithium-ion batteries

Currently, lithium-ion batteries are widely utilized in portable electronics and electric vehicle applications. Electrodes consist of micrometer-size powder-like lithium metal oxides/phosphate materials and graphite-based materials as the cathodes and anodes, respectively, due to the high-energy density and long working life. However, the micrometer-sized powder-like electrode materials result in a long lithium-ion diffusion distance and limited electronic transport rates, leading to insufficient cycling and rate performance.[87,88] To address these limitations, a promising approach is the preparation of advanced electrode materials *via* structural design and composition optimization. In this regard, design and fabrication of 1D CNF-based electrode materials is a reasonable solution to decrease the lithium-ion diffusion distance due to increased electrolyte contact and a higher surface area–volume ratio.[16,89,90] In this section, CNF-based anode and cathode materials will be discussed, focusing on the structure design and its influence on the electrochemical performance.

3.1 Carbon nanofiber-based anode materials for lithium-ion batteries

In modern LIB technology, graphite-based materials are the commercial anode materials of choice due to the advantages of low voltage potential, cycling stability, and cost-effectiveness. However, the low capacity (theoretical capacity: 372 mA h g^{-1}) and sluggish lithium-ion diffusion kinetics has limited the application of graphite-based materials in next-generation high-energy LIBs.[91,92] To fabricate high-capacity anode materials, two main strategies have been intensively studied. One is to develop more lithium-storage sites in carbonaceous materials, like porous structures, while another is to develop other non-carbon anode materials with higher theoretical capacity, such as alloy-type anodes, metal oxides and metal sulfides.[93–98] For 1D carbonaceous anode materials, CNFs have proven to be a hopeful alternative to traditionally used graphite-based anode materials, owing to the improved access to the electrolytes, fast electron transport pathways along the 3D conductive network and increased lithium storage sites.[48,84,99] In the case of alloy-type, metal oxide and metal sulfide anode materials, the fabrication of CNF-based composite anodes would enhance the lithium-ion & electron transport and solve many of the problems of these materials during cycling (*e.g.* huge volume variation during cycling, unstable solid electrolyte layer (SEI), and aggregation of the active electrode materials), simultaneously.[69,70,100] In this subsection, the CNF-based anode materials are summarized and discussed.

3.1.1 Carbon nanofiber anode materials. To the best of our knowledge, CNFs were first used as anode materials for the LIBs in the mid-2000s. Zou *et al.*,[101] and Kim *et al.*[84] reported the

Table 1 Comparison of the preparation strategies of carbon nanofibers

Preparation strategies	Chemical vapor deposition growth	Electrospun carbon nanofibers	Template-based strategies	Biomass methods
Diameter (nm)	50–200	20–1000	50–200	10–80
Length (μm)	50–100	1×10^3 to 1×10^4	1–60	1–10
Electrical conductivity (S cm^{-1})	1×10^3 to 1×10^4	1–600	1–10	0.2–2
Cost (USD per kg)	>500	N/A	N/A	30

Published on 20 June 2017. Downloaded by University of Western Ontario on 27/07/2017 20:28:34.

lithium storage performance of CNFs, which were fabricated *via* co-catalyst deoxidization and electrospinning strategies, respectively. Although the two studies show the potential applications of CNFs in the LIBs, the electrochemical performance is limited with only 220 mA h g^{-1} after 30 cycles at 0.1 mA cm^{-2} and 450 mA h g^{-1} after 2 cycles at 30 mA g^{-1}, respectively. Afterwards, many efforts have been made to improve the electrochemical performance of CNF anode materials, including heteroatom doping and fabrication of porous structures.

For the heteroatom doping of carbonaceous materials, nitrogen-doping has proven to be a popular strategy to enhance the electrical conductivity and increase lithium storage capacity *via* the heteroatomic defects,[22] which are usually realized by the treatment of carbonaceous material with nitrogen-containing precursors (*e.g.* NH_3, melamine and urea).[102–104] Nan and co-workers[102] fabricated nitrogen-doped porous carbon nanofibers (NPCNFs) *via* combining electrospinning and NH_3 treatment. During the electrospinning process, melamine was added into the PAN-based precursor solution, acting as the resource of nitrogen. After the carbonization of electrospun nanofibers, nitrogen-doped carbon nanofibers (NCNFs) would be obtained, which were further treated under an atmosphere of N_2/NH_3 to yield the NPCNFs. As shown in Fig. 2A, the NPCNFs form a 3D interconnected network with a porous structure due to the activation of NH_3. In addition, after the treatment of NH_3, the NPCNFs display high nitrogen-doping as shown in Fig. 2B, significantly greater than that of NCNFs and CNFs prepared without melamine and NH_3 treatment. Owing to the high nitrogen content and the porous structure, the NPCNFs present an improved cycling performance of 1150 mA h g^{-1} after 50 cycles at a current density of 50 mA g^{-1} and rate-capabilities superior to that of CNFs and NCNFs (Fig. 2C and D), indicating that the nitrogen doping in CNFs increases the lithium storage capacity and enhance electronic conductivity. Although the post-treatment of CNFs with nitrogen-containing precursors could enhance the electrochemical performance, the post-treatment strategy would increase the complexity and cost of the preparation process. Wang and co-workers[105] realized the fabrication of N-doped CNFs *via* direct carbonization of N-rich conducting polymer PPy nanofibers, which were prepared *via* the oxidative template assembly route. As the PPy nanofibers contain a high nitrogen content (around 16 wt%), N-doped CNFs were obtained after the carbonization process, retaining a high nitrogen content between 13 and 15 wt%. Furthermore, carbonization at different periods of time led to CNFs with unique nitrogen-doped structures. The nitrogen in the N-doped CNFs can be assigned to three types, N-6 (pyridinic N), N-5 (pyrrolic- or pyridonic-N) and N-Q (graphitic N), whose content in the N-doped CNFs with different treatment times is different from each other. By comparing the electrochemical performance of N-doped CNFs with that of different nitrogen-doping types, the N-6 pyridinic functionality is believed to be the most beneficial in increasing the capacity of CNF anode materials.

In addition to the heteroatom doping strategy, the preparation of porous structures is another rational strategy used to enhance the electrochemical performance of CNFs. The preparation of these structures is usually achieved through the catalytic chemical vapor deposition growth, template-based and activation strategies. Since the cup-stacked CNFs can be

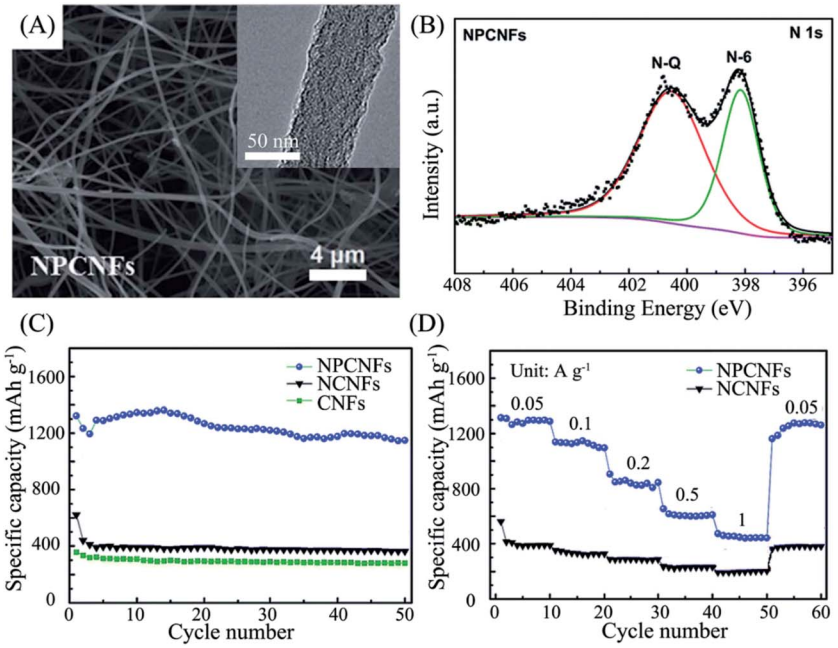

Fig. 2 (A) SEM and TEM images and (B) N1s XPS spectra of N-doped porous carbon nanofibers; (C) cycle performance at a current density of 50 mA g^{-1} and (D) rate performance at various current densities from 50 to 1000 mA g^{-1} of NPCNFs, NCNFs and CNFs. Reproduced with permission,[102] Copyright© 2014 Royal Society of Chemistry.

Published on 20 June 2017. Downloaded by University of Western Ontario on 27/07/2017 20:28:34.

fabricated *via* the catalytic chemical vapor deposition growth, porous CNFs based on the cup-stack design have been fabricated by Deng *et al.*[106] and Subramanian *et al.*,[107] respectively, as anode materials for LIBs with improved lithium storage performance. For the template-based strategy, hard- or soft-templates (*e.g.* SiO_2, poly-L-lactic acid (PLLA) and poly(methyl methacrylate) (PMMA)) are usually introduced into the preparation process, acting as the artificial sections to produce pores in the CNF materials after removal by etching or decomposition at high temperature.[105,108–112] Among the templates, SiO_2 is a templating material widely utilized to prepare porous carbon structures.[113,114] Ji *et al.*[108] have prepared porous CNFs *via* the use of a PAN–SiO_2 solution as an electrospinning precursor solution, following by the electrospinning and carbonization processes and subsequent removal of SiO_2 by etching with HF. Ascribed to the porous structure, the porous CNFs displayed an improved lithium storage capacity (454 mA h g^{-1} after 10 cycles) over that of the non-porous CNFs (400 mA h g^{-1} after 10 cycles) when cycled at a current density of 50 mA g^{-1}, suggesting that the fabrication of pore networks in CNFs can increase the lithium storage sites and reversible capacity. Different from the template strategy, the activation process utilizes activation agents (usually, KOH) to react with CNFs and to fabricate the porous structures.[48,77,99,115] Qie and co-workers[48] have fabricated N-doped porous carbon nanofiber webs (CNFWs) *via* carbonization of PPy nanofibers with KOH as the activation agents. As shown in Fig. 3A and B, the obtained nanofibers display porous structures with abundant micropores and a 3D interconnected network, whilst presenting a high content of nitrogen doping resulting from the high nitrogen content in PPy nanofibers, similar to Wang *et al.*'s previously discussed work.[112] Comparing the electrochemical performance of the N-doped porous CNFs in Qie *et al.*'s work and the N-doped CNFs in Wang *et al.*'s work prepared from the same precursor nanofibers, the highly porous structure further improves the capacity and cyclability at high current densities, 943 mA h g^{-1} after 600 cycles at a high current density of 2 A g^{-1} in addition to excellent rate performance at current densities from 0.1 to 20 A g^{-1} (Fig. 3C and D), implying that the highly porous structure cannot only increase lithium storage sites but also enhance the lithium diffusion rate. Apart from KOH, oxygen can also be used as an activation agent to produce porous carbonaceous materials. As shown in Fig. 4A and B, Li and co-workers[99] present highly porous carbon nanofibers (HPCNFs) *via* carbonization of electrospun PAN nanofibers under a mixed atmosphere of Ar and trace amount of air. The reaction between carbon and oxygen would lead to formation of pores in the CNFs. Benefiting from the increased lithium storage sites and decreased lithium-ion diffusion length, the HPCNFs display significantly increased lithium storage capacity (1780 mA h g^{-1} after 40 cycles at a current density of 0.05 A g^{-1}) and rate capability, compared with the CNFs without air activation (Fig. 4C and D).

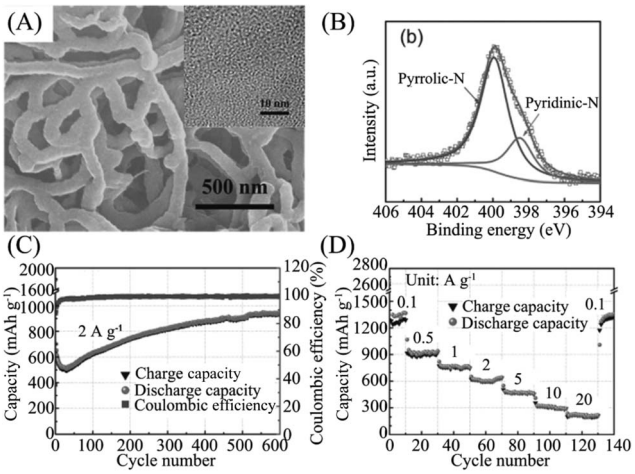

Fig. 3 (A) SEM and TEM images and (B) N1s XPS spectra of N-doped porous carbon nanofiber webs (CNFWs); (C) cycle performance at a current density of 2 A g^{-1} and (D) rate performance at various current densities from 0.1 to 20 A g^{-1} of. Reproduced with permission,[48] Copyright© 2012 Wiley.

As most of the porous CNFs are made of amorphous carbon, which exhibits lower electronic conductivity than graphitic carbon, the electrochemical activity at higher current densities may be limited. To realize graphitic porous CNFs, Chen *et al.*[116–118] and Zhang *et al.*[119] applied Ni and Fe nanoparticles as a sacrificial catalyst during the carbonization of electrospun polymer nanofibers, respectively. Fig. 5A and B show the structure of the functionalized porous graphitic CNFs (FPG-CNFs) prepared with Fe nanoparticles as the sacrificial catalyst, displaying numerous graphitic nanospheres in the CNFs and plenty of nanopores on the surface of nanospheres after the removal of Fe_3N nanoparticles with HNO_3. Furthermore, the HNO_3 treatment also functionalizes the graphitic porous CNFs with oxygenated groups, which are active for faradaic reactions with lithium-ion. Benefiting from strengthened electronic conductivity of graphitic layers as well as numerous lithium-ion intercalation sites due to the nanopores and oxygenated groups, as shown in Fig. 5C and D, the FPG-CNFs present improved rate performance and cycling performance (609 mA h g^{-1} after 100 cycles at a high current density of 1 A g^{-1}), compared to the CNFs and functionalized CNFs (F-CNFs). In addition, the CNFs also combined with other carbonaceous nanostructures (*e.g.* carbon nanotubes[120] and graphene[55]) is another promising strategy to increase lithium storage sites and enhance lithium-ion & electron diffusion, simultaneously.

Obviously, the number of lithium-intercalation sites and the lithium-ion & electron transport rate plays crucial roles in the electrochemical performance of CNF anode materials for LIBs. Table 2 summarizes the morphology (*i.e.* diameter and surface area) and the corresponding electrochemical performance of CNFs. To realize higher specific capacity, it is rational to create more pores or defects CNFs acting as lithium storage sites. However, the resulting high surface area also leads to high irreversible capacity, mainly owed to the formation of a thick SEI layer on the large contact area of electrolytes and electrodes and highly limiting the practical application in commercial lithium-ion batteries. Therefore, it is required to balance between the high reversible capacity and irreversible lithium consumption *via* designing porous structures. In addition, the electrical conductivity and lithium-ion diffusion kinetics of

Published on 20 June 2017. Downloaded by University of Western Ontario on 27/07/2017 20:28:34.

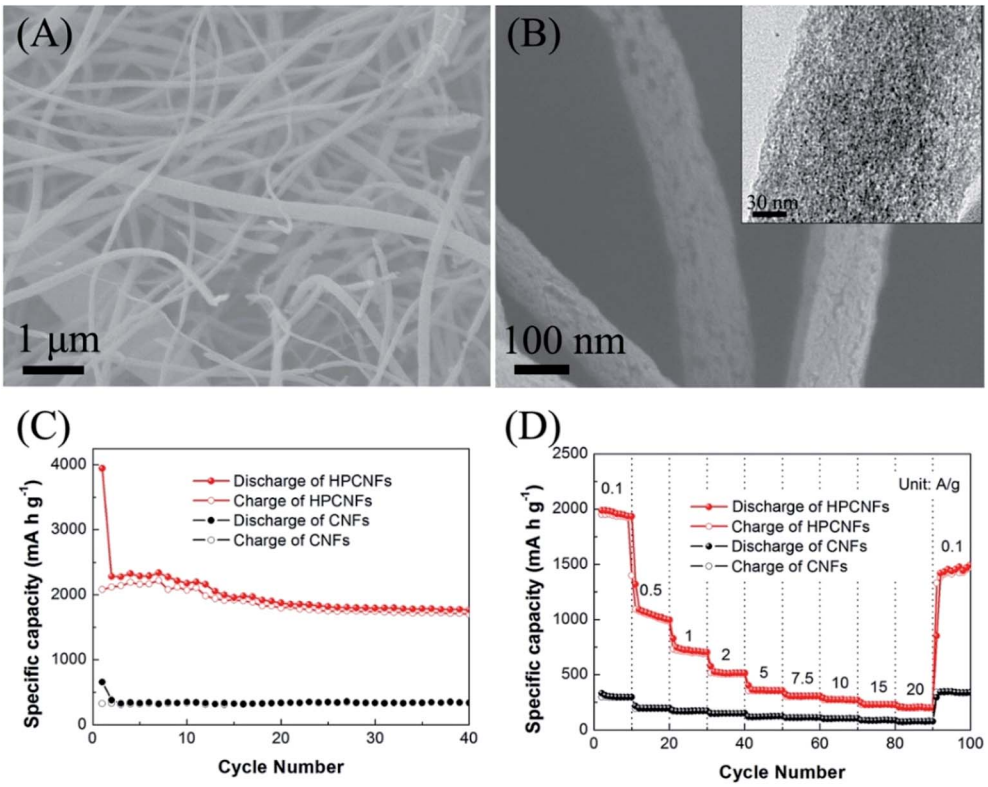

Fig. 4 (A) & (B) SEM and TEM images of the highly porous carbon nanofibers (HPCNFs) and (C) cycle performance at a current density of 0.05 A g^{-1} and (D) rate performance at various current densities from 0.1 to 20 A g^{-1} of HPCNFs and CNFs. Reproduced with permission,[99] Copyright© 2015 Elsevier.

CNFs are also determined by the pore & defect structures. A highly porous structure provides good access of the electrolyte to the electrode surface and speeds up lithium transport. Nevertheless, a porous structure with pores & defects would damage the crystallinity and electrical conductivity. As a result, the electron and lithium-ion transport in CNFs can be affected by the porous structure, finally acting on the electrochemical performance. Furthermore, the porous structure also has an impact on the mechanical properties and decrease the mechanical strength of CNFs, which is bad for practical application. Therefore, the rational structural design of CNFs should consider the influence of pores & defects on the lithium storage

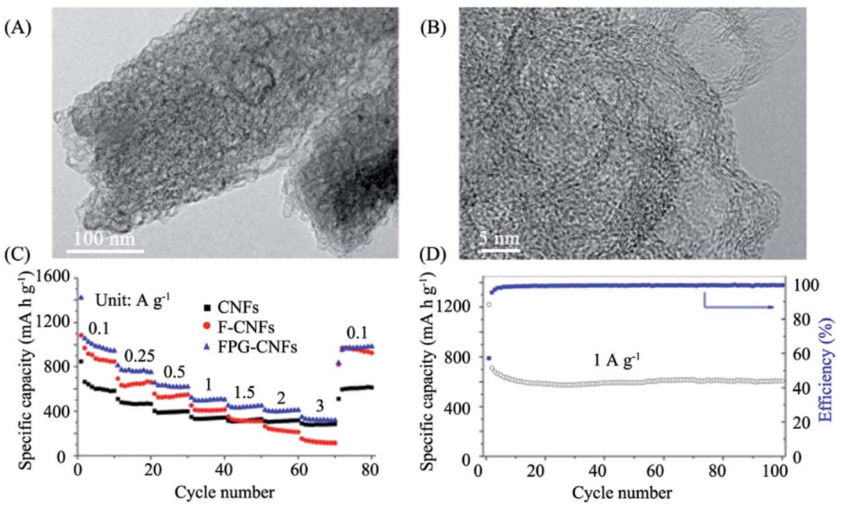

Fig. 5 (A) & (B) TEM images of the functionalized porous graphitic CNFs (FPG-CNFs), (C) rate performance of FPG-CNFs, F-CNFs, and CNFs and (D) cycle performance of FPG-CNFs cycled at 1 A g^{-1}. Reproduced with permission,[119] Copyright© 2013 Elsevier.

 This journal is © The Royal Society of Chemistry 2017

Published on 20 June 2017. Downloaded by University of Western Ontario on 27/07/2017 20:28:34.

Table 2 Electrochemical performance of carbon nanofibers as anodes for LIBs

Materials	Preparation strategy	Diameter & surface area	Electrochemical performance	Rate
CNFs[84]	Electrospinning	250 nm/N/A	450 mA h g^{-1} after 2 cycles	30 mA g^{-1}
CNFs[62]	Co-catalyst deoxidization	100 nm/~100 m^2 g^{-1}	220 mA h g^{-1} after 30 cycles	0.1 mA cm^{-2}
N-Doped porous CNFs[102]	Electrospinning, melamine and NH_3 treatment	Tens–hundreds nm/1198 m^2 g^{-1}	1150 mA h g^{-1} after 50 cycles	50 mA g^{-1}
N-Doped CNFs[104]	Electrospinning, urea treatment	~500 nm/381 m^2 g^{-1}	576 mA h g^{-1} after 50 cycles	30 mA g^{-1}
N-Doped CNFs[103]	Chemical vapor deposition	~60 nm/108.1 m^2 g^{-1}	300 mA h g^{-1} after 50 cycles	186 mA g^{-1}
N-Doped CNFs[112]	Oxidative template assembly	70–90 nm/N/A	605 mA h g^{-1} after 10 cycles	100 mA g^{-1}
Porous CNFs[106]	Chemical vapor deposition	100–200 nm/N/A	260 mA h g^{-1} after 25 cycles	100 mA g^{-1}
Porous CNFs[107]	Chemical vapor deposition	20–30 nm/100 m^2 g^{-1}	170 mA h g^{-1} after 10 cycles	3 A g^{-1}
Porous CNFs[108]	Electrospinning, SiO_2 template	~500 nm/91.8 m^2 g^{-1}	454 mA h g^{-1} after 10 cycles	50 mA g^{-1}
Porous CNFs[111]	Electrospinning, PLLA template	200–300 nm/235 m^2 g^{-1}	435 mA h g^{-1} after 10 cycles	50 mA g^{-1}
Porous CNFs[109]	Electrospinning, $ZnCl_2$ template	250 nm/438 m^2 g^{-1}	430 mA h g^{-1} after 10 cycles	50 mA g^{-1}
Porous CNFs[105]	Electrospinning, SiO_2 template	Tens–hundreds nm/950 m^2 g^{-1}	445 mA h g^{-1} after 50 cycles	50 mA g^{-1}
Porous CNFs[77]	Biomass method, KOH activation	20–30 nm/1235.58 m^2 g^{-1}	857.6 mA h g^{-1} after 100 cycles	100 mA g^{-1}
Porous CNFs[99]	Electrospinning, air activation	~400 nm/583 m^2 g^{-1}	1780 mA h g^{-1} after 40 cycles	50 mA g^{-1}
N-Doped porous CNFs[48]	Oxidative template assembly, KOH activation	60–80 nm/2381 m^2 g^{-1}	943 mA h g^{-1} after 600 cycles	2 A g^{-1}
Graphitic porous CNFs[116]	Electrospinning, Ni nanoparticle template	~250 nm/67.5 m^2 g^{-1}	750 mA h g^{-1} after 50 cycles	50 mA g^{-1}
Graphitic hollow porous CNFs[117]	Electrospinning, Ni nanoparticle template	~200 nm/N/A	969 mA h g^{-1} after 100 cycles	50 mA g^{-1}
Graphitic porous CNFs[118]	Electrospinning, Ni nanoparticle template	~200 nm/538 m^2 g^{-1}	1560 mA h g^{-1} after 40 cycles	100 mA g^{-1}
Graphitic porous CNFs[119]	Electrospinning, Fe nanoparticle template	100–300 nm/198 m^2 g^{-1}	609 mA h g^{-1} after 100 cycles	1 A g^{-1}
CNFs–CNTs[120]	Electrospinning, chemical vapor deposition	~200 nm/1840 m^2 g^{-1}	1150 mA h g^{-1} after 70 cycles	100 mA g^{-1}
CNFs–graphene[55]	Chemical vapor deposition	~20 nm/315 m^2 g^{-1}	667 mA h g^{-1} after 30 cycles	0.12 mA cm^{-2}

performance (including reversible and irreversible capacity), electronic & ionic conductivity and mechanical properties and optimize the effect on all parts to realize the optimal electrochemical performance and practical application in commercial lithium-ion batteries.

3.1.2 Carbon nanofiber-based composite anode materials for lithium-ion batteries. Due to the capacity limitation of graphite-based anode materials, many efforts have been devoted to other types of anode materials, including alloys, metal oxides, and metal sulfides.[97] Although these anode materials display higher lithium storage capacity, the cyclability is inferior and inadequate for many practical applications. For alloy-type anodes (*e.g.* Si, Ge, and Sn), the materials undergo large volume variation, resulting in cracking and pulverization during cycling, which can cause electrode particles to become electrochemically inactive and promotes the continuous growth of the SEI layer which leads to rapid capacity degradation and low coulombic efficiency.[95,98] In the case of metal oxides and metal sulfides, like TiO_2, SnO_2, Fe_2O_3, and MoS_2, the low lithium-ion diffusion rate and poor electrical conductivity limit the electrochemical activity and lithium storage performance, in addition to some of these anode materials undergoing huge volume changes and fast capacity deterioration.[121,122] To solve the issues of these anode materials, CNFs may serve as a promising substrate to accommodate the volume change, enhance the ionic & electronic transport and control the nanostructures of these anode materials *via* designing and fabricating rational structures. These designs include the outer-surface anchoring and encapsulation type structures.

The outer-surface anchoring structure is usually fabricated by growing active anode materials on the surface of the CNFs *via* magnetron sputtering,[100] electrodeposition,[123–125] electrophoretic deposition,[126] chemical vapor growth,[46,127] hydrothermal/solvothermal growth,[128–131] and solution-based strategies.[132,133] To overcome the huge volume variation and low electronic conductivity of silicon anode materials, Cui and co-workers[46] have fabricated carbon–silicon core–shell nanowires *via* direct chemical vapor deposition of amorphous Si on the surface of the commercial CNFs. As shown in Fig. 6A, amorphous Si is uniformly coated on the surface of CNFs, which has a greater compatibility for the huge volume change compared to crystalline Si, and displays good structural stability during cycling (Fig. 6B). Moreover, the CNFs function as a stable mechanical support for amorphous Si, able to provide fast electronic transport pathways for the entire anode material. Owning to the strengthened structural stability and electronic conductivity, the C–Si core–shell nanowires present good cycle performance as shown in Fig. 6C and D, high reversible capacities of 1300 and 800 mA h g^{-1} with good cycling stability observed at the current densities of 0.5 and 2.5 A g^{-1}, respectively. The enhanced performance indicates that the outer-surface anchoring structure of active anode materials is feasible to improve the electrochemical performance of alloy anode materials. In addition to the growth of amorphous anode

Published on 20 June 2017. Downloaded by University of Western Ontario on 27/07/2017 20:28:34.

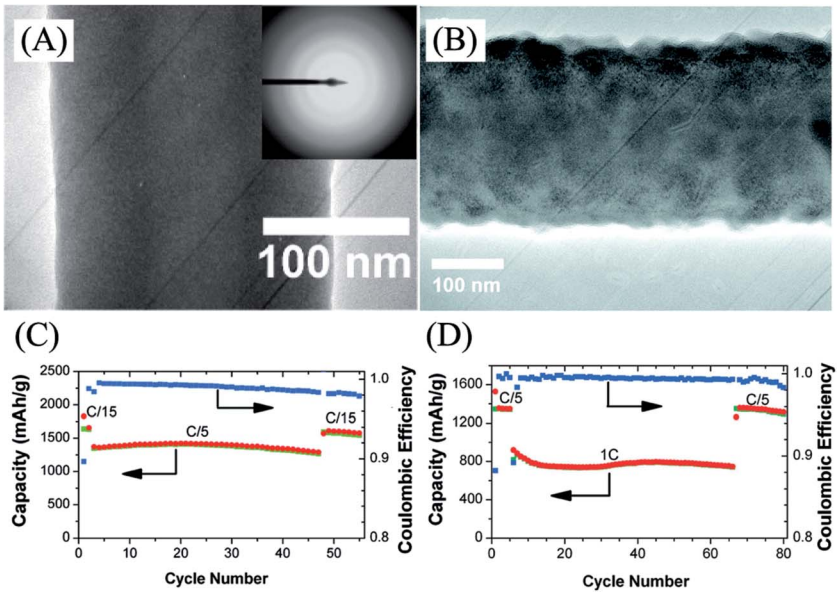

Fig. 6 (A) TEM and selected area electron diffraction (SAED) images of C–Si core–shell nanowires and (B) TEM image of C–Si core–shell nanowires after 5 cycles; (C) & (D) cycle performance of C–Si core–shell nanowires cycled at different rates between 0.1 and 1 V *vs.* Li/Li^+. Reproduced with permission,[46] Copyright 2009 American Chemical Society.

materials on the surface of CNFs, non-carbon anode materials with nanoparticle and nanosheet morphologies have been fabricated on the surface to form the outer-surface anchoring structure, showing improved electrochemical performance. Zhang and co-workers[133] have prepared Mn-based transition metal oxide (TMO) nanoparticles anchored to the surface of CNFs to form a nanocable structure (*i.e.* CNF@MnO and CNF@$CoMn_2O_4$) *via* a solution-based method and subsequent thermal treatment. Fig. 7A and B show the morphology of the CNF@MnO and CNF@$CoMn_2O_4$ nanocables, consisting of MnO and $CoMn_2O_4$ nanocrystals homogeneously distributed on the surface of the CNFs without any obvious space between the core and shell layers, indicating a tightly anchored structure. The outer-surface anchoring structure of oxide anode materials displays many advantages, including the stabilizing effect of the CNF supporting structures on the metal oxides, which accommodates the large volume changes; a tight anchoring structure to prevent the aggregation of metal oxide nanoparticles during cycling and excellent electronic conductivity of the CNFs to enhance overall electron transport in the nanocable electrodes. Owing to the unique structure, as displayed in Fig. 7C and D, the two materials show good cyclability and high coulombic efficiency (735 and 870 mA h g^{-1} after 150 cycles at a current density of 200 mA g^{-1} for the CNF@MnO and CNF@$CoMn_2O_4$, respectively). Additionally, metal sulfide nanosheets have been prepared on the surface of the CNFs to improve the electrochemical performance, such as carbon nanofibers decorated with MoS_2 nanosheets (denoted as CNFs@MoS_2) fabricated by Zhou and co-workers.[129] Fig. 8A presents the morphology of the CNFs@MoS_2 with mesoporous MoS_2 nanosheets grown on the surface of the template-prepared CNFs *via* the solvothermal method. Furthermore, high-resolution TEM images confirm the expanded interlayer spacing of MoS_2 nanosheets from the 0.632 nm of bare MoS_2 to 0.684 nm, suggesting higher electrochemical activity. Benefiting from the enhanced electronic and ionic transport of the structure and protective effect of the CNFs on the volume change of MoS_2 during cycling, the material displays improved rate performance (Fig. 8B) and a long cycle-life performance of 688 mA h g^{-1} after 300 cycles at a current density of 1 A g^{-1} (Fig. 8C).

On the other hand, the encapsulation-type structure is another reasonable design *via* embedding of active anode materials with nanoparticle, nanosheet, or nanowire morphologies in the CNFs to improve the electrochemical performance. Differing from the outer-surface anchoring structure, which alleviates the stress resulting from the volume change of active materials *via* downsizing of the active materials to nanoscale particles and the supporting effect of CNFs, the encapsulation structure can further accommodate the large volume variation through the surrounding layers of CNFs to stabilize the structure during cycling. In addition, the three-dimensional (3D) interconnected networks formed by the CNFs display increased electronic conductivity and good access to electrolytes. The main strategy to fabricate encapsulation structure is the electrospinning method,[66] whilst the obtained CNF-based composite nanofibers can be modified through other methods, like CVD and other post-treatment (*e.g.* etching and heat treatment).[74,134–136] Since alloy anode materials suffer from huge volume change during cycling and fast capacity decay, Li and co-workers[70] have fabricated germanium nanoparticles encapsulated in CNFs (Ge@CNFs) to accommodate the volume variation and improve the cyclability. Fig. 9A show the encapsulation structure of the Ge@CNFs, forming the 3D interconnected network, which has shown excellent structural stability after 100 cycles (Fig. 9B). Ascribed to the encapsulating structure and the enhanced electronic & ionic transport, a high

 This journal is © The Royal Society of Chemistry 2017

Published on 20 June 2017. Downloaded by University of Western Ontario on 27/07/2017 20:28:34.

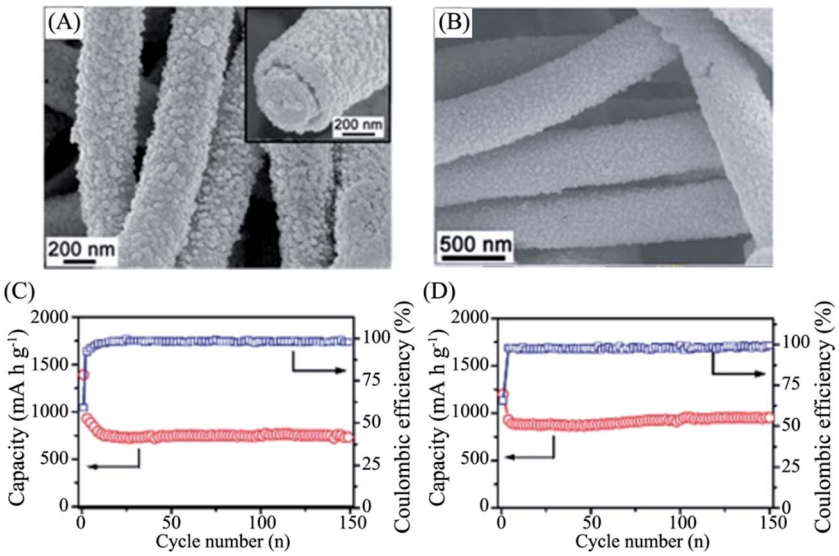

Fig. 7 SEM images of the CNF@MnO (A) and the CNF@$CoMn_2O_4$ (B); cycle performance of the CNF@MnO (C) and the CNF@$CoMn_2O_4$ (D) cycled at a current density of 200 mA g^{-1}. Reproduced with permission,[133] Copyright© 2014 Royal Society of Chemistry.

reversible capacity of 1420 mA h g^{-1} after 100 cycles at 0.15C and excellent rate performance have been realized (Fig. 9C and D). This example illustrates the ability of the encapsulation structure to enhance the electrochemical performance of non-carbon anode materials. This type of encapsulation structure has been widely applied to enhance the cyclability and rate capability of other anode materials, including Si,[137] SnO_2,[138] Fe_2O_3,[139] CoO,[140] and TiO_2.[141,142] In addition, to further accommodate the volume change and stabilize the structure during cycling, the inside encapsulation structures with the additional carbon layers or the porous structures have been designed and synthesized to further enhance performance.[69,74,135,136,143–146] Fu and co-workers[135] have fabricated Si nanoparticles encapsulated in CNFs (Si@CNF) coated with additional carbon layers *via* the CVD process (Si@CNF–C), which showed good structural stability during cycling (Fig. 10A and B). As shown in Fig. 10C, the Si@CNF–C composite with additional carbon coating layers displays better cycling performance compared to the Si@CNF,

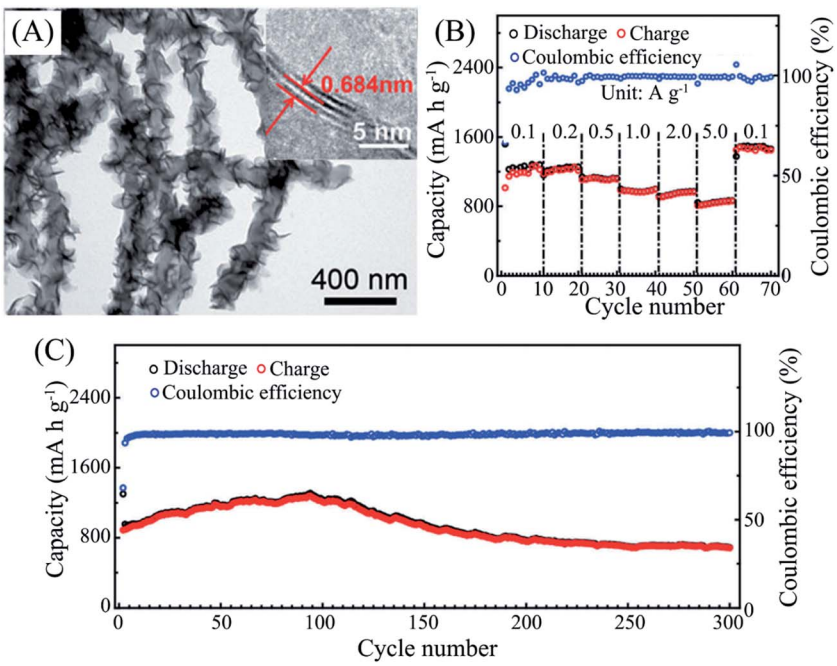

Fig. 8 (A) TEM and HRTEM images of the CNF@MoS_2; (B) & (C) cycle performance of the CNF@MoS_2: (B) rate performance at different current densities from 0.1 to 5 A g^{-1} and (C) long-life cycle performance at the current density of 1 A g^{-1}. Reproduced with permission,[129] Copyright© 2014 Wiley.

Published on 20 June 2017. Downloaded by University of Western Ontario on 27/07/2017 20:28:34.

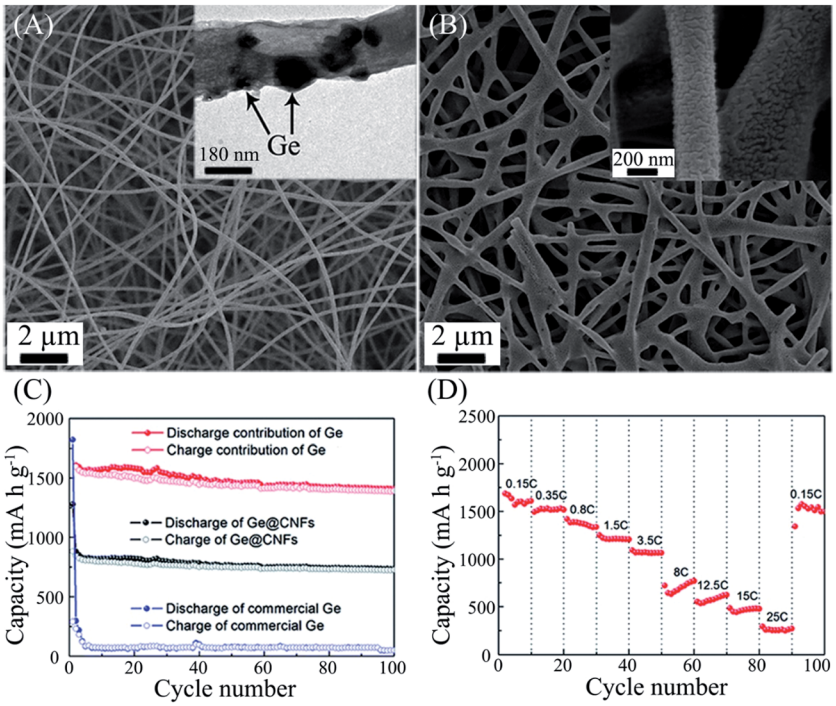

Fig. 9 SEM images of the Ge@CNFs before cycling (A) and after cycles (B), the inset in (A): TEM image of Ge@CNFs. (C) & (D) Electrochemical performance of Ge–CNFs and commercial Ge powder electrodes cycled between 0.005 V and 1.2 V *vs.* Li^+/Li. (C) Capacity–cycle number curves of Ge–CNFs and commercial Ge powder electrodes at a cycling rate of 0.15C; (D) discharge capacity of Ge–CNF electrodes as a function of discharge rate (0.15–25C). Reproduced with permission,[70] Copyright© 2014 Royal Society of Chemistry.

suggesting that the additional carbon coating layers is crucial to improving the cyclability. However, the weight content of the active material in the composite is 10 wt%, which needs to be increased to meet the demand of high capacity. To realize an increase in the weight content of Si in the composite, Xue *et al.*[143] have prepared carbon coated Si nanoparticles embedded in the CNFs (Si@C/CNF) with 30 wt% (Fig. 10D). Furthermore, as presented in Fig. 10E and F, the electrodes formed with ground Si@C/CNF show better capacity retention than the Si nanoparticles embedded in the CNFs (Si/CNF) and the Si@C/CNF mat, emphasizing the accommodating effect of the additional carbon layer on the Si nanoparticles and the stabilization effect of the polymer binder. Similar to the elastic characteristics of the additional carbon coating layers, the fabrication of a porous structure is another reasonable way to prevent the anode materials from collapsing.[147] In recent times, Yu *et al.*[69,144] have fabricated two rational capsulation structures with porous structures that have been fabricated by Sn nanoparticles embedded in the porous CNFs. By introducing PMMA as sacrificial templates, Sn nanoparticles encapsulated in porous multi-channel carbon microtubes (SPMCTs) were prepared after the decomposition of PMMA (Fig. 11A and B). On the other hand, Sn@carbon nanoparticles encapsulated in bamboo-like hollow carbon nanofibers were fabricated through coaxial electrospinning with the mineral oil as the core template (Fig. 11D and E). The additional empty space in the structures and carbon coating layers on the surface of the Sn nanoparticles can accommodate the volume change of Sn and lead to formation of stable SEI layers and facilitate the ionic transport. Both anode materials presented excellent cycle stability (Fig. 11C and F). In addition to the modification to improve the structure and cycle stability of anode materials, it is vital to increase the electronic conductivity to further enhance the rate performance *via* introducing highly electronic conductive materials (*e.g.* heteroatom-doping, carbon nanotubes, graphene, *etc.*).[148–151] Zhang *et al.*[148] reported amorphous SnO_x nanoparticles embedded in carbon nanofiber/carbon nanotube composites (SnO_x/CNF/CNT) with the typical core–shell structure prepared *via* the electrospinning, consisting of SnO_x@CNF as the core and CNTs embedded in the shell (Fig. 12A–C). Benefiting from the enhanced electronic conductivity of the 3D interconnected conductive network and the CNT shell structure, shown in Fig. 12D and E, the SnO_x/CNF/CNT presented good rate and excellent cycling performance at a high current density of 2 A g^{-1} (a high reversible capacity of 405 mA h g^{-1} after 300 cycles).

As summarized in Table 3, the fabrication of CNF-based composites is one reasonable structural design to improve the electrochemical performance of non-carbon anode materials for the LIBs, due to its excellent electronic and good access to the electrolytes based on the 3D interconnected CNF networks. In addition, CNFs are capable of acting as a stress buffer to accommodate the volume change of anode materials during cycling and improve cycling stability. Furthermore, the layers of CNFs can also contribute to the formation of a stable SEI layer and reduce continuous consumption of the electrolyte during

 This journal is © The Royal Society of Chemistry 2017

Published on 20 June 2017. Downloaded by University of Western Ontario on 27/07/2017 20:28:34.

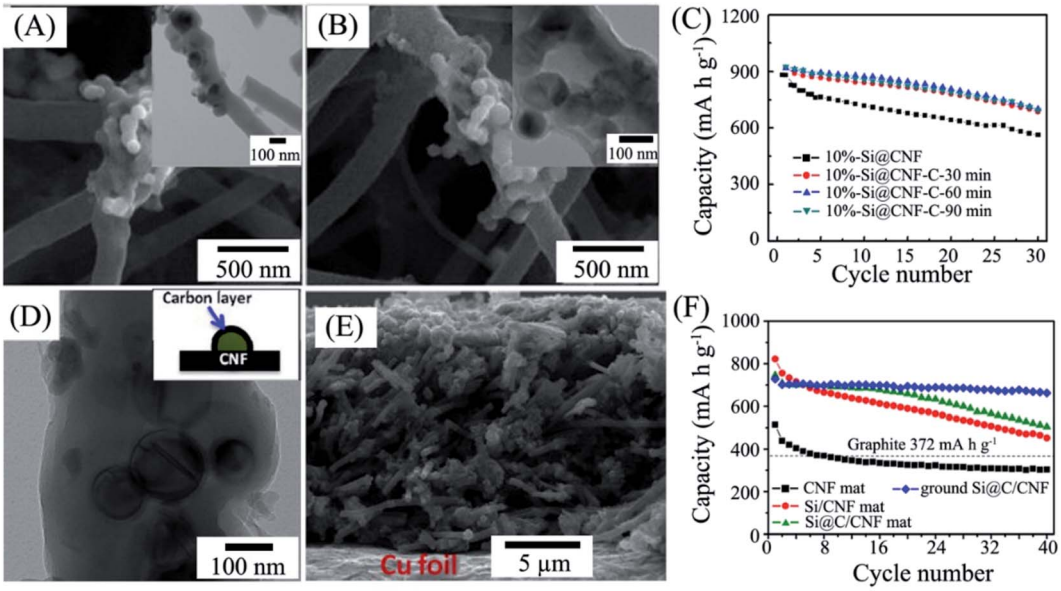

Fig. 10 SEM and TEM images of 10 wt% Si@CNF–C composites with a coating time of 90 min before cycling (A) and after cycles (B); (C) cycle performance of 10 wt% Si@CNF–C composites with different coating times cycled between 0.01 V and 2 V *vs.* Li^+/Li at the current density of 50 mA g^{-1}. Reproduced with permission,[135] Copyright© 2013 Elsevier. (D) TEM image of Si@C/CNF and (E) cross-sectional SEM image of electrodes of Si@C/CNF; (F) cycle performance of CNF mat, Si/CNF mat, Si@C/CNF mat and ground Si@C/CNF cycled between 0.02 V and 2 V *vs.* Li^+/Li at the current density of 50 mA g^{-1}. Reproduced with permission,[143] Copyright© 2013 Elsevier.

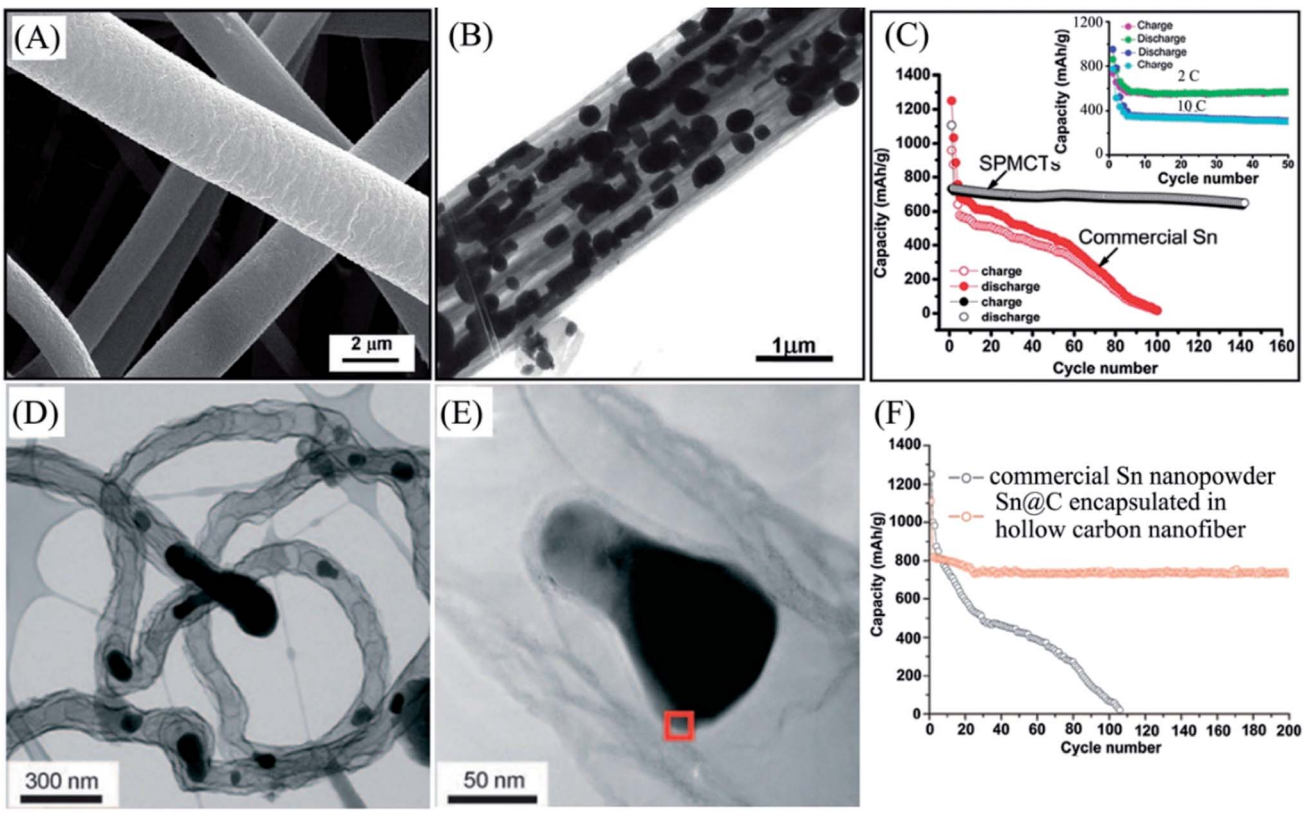

Fig. 11 (A) SEM and (B) TEM images and (C) cycle performance of Sn particles encapsulated in porous multichannel carbon microtubes (SPMCTs) at different current densities. Reproduced with permission,[69] Copyright© 2009 American Chemical Society. (D) & (E) TEM images and (F) cycle performance of Sn@C encapsulated in hollow carbon fibers. Reproduced with permission,[144] Copyright© 2009 Wiley.

Published on 20 June 2017. Downloaded by University of Western Ontario on 27/07/2017 20:28:34.

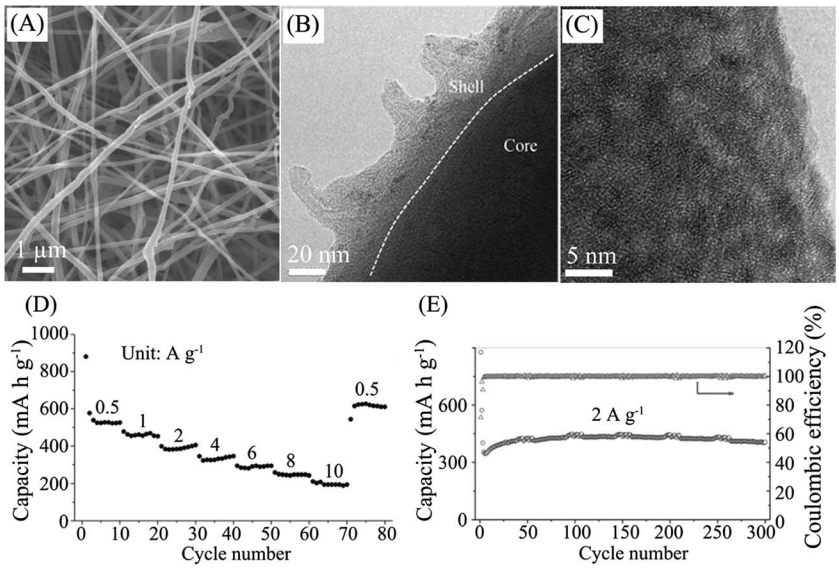

Fig. 12 (A) SEM, (B) TEM and (C) HRTEM images, (D) rate performance and (E) long-life cycle performance at the current density of 2 A g^{-1} of SnO_x/CNF/CNT composites. Reproduced with permission,[148] Copyright© 2015 Wiley.

cycling. However, the high specific surface area of CNF-based anode materials would cause high irreversible capacity due to the decomposition of the electrolyte on the surface and formation of the SEI layer. Therefore, it is crucial to design rational structure of CNF-based anode materials to balance the enhancement of electron & ion transport and structural stability between the surface area. Moreover, the specific capacity of CNFs is usually lower than that of non-carbon anode materials. The weight content of CNFs in the composite anode materials is one key factor to influence the overall capacity of the CNF-based anode materials. Although it is required to prepare composite anode materials with a high enough content of CNFs to stabilize the overall structure during cycling. Consequently, it is reasonable to adjust the content and design morphology of CNF-based anode materials to realize high electrochemical performance, structural stability and low irreversible capacity, simultaneously.

3.2 Carbon nanofiber-based composite cathode materials for lithium-ion batteries

Currently, the research of cathode materials for LIBs is focused on lithium-transition metal oxides (*e.g.* $LiCoO_2$, $LiMn_2O_4$, $LiFePO_4$), transition metal oxides (*e.g.* V_2O_5) and transition metal sulfides (FeS and FeS_2).[152,153] Among these cathode materials, $LiFePO_4$ holds promising potential in the application of next-generation high-energy lithium-ion batteries, due to the excellent cycling stability, abundant resources, and environmental benignity.[154] Nevertheless, the sluggish mass and charge transport in $LiFePO_4$ limits the electrochemical activity and electrochemical performance. To overcome the limitations, various strategies have been applied to fabricate nanosized electrode materials and efficient electron conductive pathways to enhance ionic and electronic conductivity, such as the fabrication of CNF–$LiFePO_4$ composites.[155–158] To develop a superior cathode material, Zhu and co-workers[155] synthesized carbon-coated singly-crystalline $LiFePO_4$ (LFP) nanowires *via* an electrospinning method. As presented in Fig. 13A and B, the single crystalline LFP nanowires grow along the *c* axis and display a short mass transport length along the *a* and *b* directions, coated by carbon layers to form 3D interconnected electronic conductive networks. The rapid lithium-ion and electron transport of the structure led to excellent rate performance (Fig. 13C) and improved cycling stability at a high current density of 1C in addition to excellent thermal stability at a high temperature of 60 °C (Fig. 13D). In the case of other cathode materials, such as Li_2MnSiO_4,[159] $LiFe_{1-y}Mn_yPO_4$,[160] $Li_2Mn_{0.8}Fe_{0.2}SiO_4$ (ref. 161) and $LiNi_{0.5}Mn_{1.5}O_4$,[162] the introduction of CNFs to form composite anode materials is also able to improve the electrochemical performance. Additionally, different from the traditional cathode materials, the transition metal sulfide cathode materials (*e.g.* FeS and FeS_2) suffer from issues attributed to long-chain lithium polysulfides formed during cycling, including shuttle effects and side reactions with electrolytes.[163,164] Zhu and co-workers[165] fabricated an Al_2O_3-coated FeS_2@carbon fiber material *via* a electrospinning method and an atomic layer deposition (ALD). Fig. 14A and B display the morphology of the FeS_2@carbon fiber and the Al_2O_3-coated FeS_2@carbon fiber, respectively, presenting FeS_2 encapsulated in the carbon nanofibers. Moreover, owing to the protection of the Al_2O_3 coating layers, FeS_2 nanoparticles remain embedded in the CNFs and show excellent structural stability during cycling as shown in Fig. 14C. In addition, the coated materials resulted in improved cycling performance at a current density of 200 mA g^{-1} (Fig. 14D, 530 mA h g^{-1} after 100 cycles with a low capacity rate of 0.12% per cycle). Furthermore, the electrodes show high energy density and reach 840 and 1110 W h kg^{-1} based on the electrode and active material, respectively, holding great promise for potential application in next-generation high-energy lithium-ion batteries.

 This journal is © The Royal Society of Chemistry 2017

Published on 20 June 2017. Downloaded by University of Western Ontario on 27/07/2017 20:28:34.

Table 3 Electrochemical performance of carbon nanofiber-based composites as anodes for LIBs

Materials	Preparation strategy	Diameter & surface area	Active material & weight content	Electrochemical performance	Rate
CNFs@amorphous Si nanowires[46]	Chemical vapor deposition (CNFs and Si)	~200 nm/N/A	Si, ~75 wt%	800 mA h g^{-1} after 60 cycles	2.5 A g^{-1}
CNFs@Si nanowires[100]	Chemical vapor deposition (CNFs)–magnetron sputtering (Si)	80–240 nm/N/A	Si, ~50 wt%	2500 mA h g^{-1} after 88 cycles	1C
Ge nanowires on CNFs[127]	Electrospinning, chemical vapor deposition	~200 nm/N/A	Ge, 50.4 wt%	1520 mA h g^{-1} after 100 cycles	0.1C
CNF@MnO nanocables[133]	Template method (CNFs)–solution method (MnO)	~300 nm/N/A	MnO, 76 wt%	735 mA h g^{-1} after 150 cycles	200 mA g^{-1}
CNF@$CoMn_2O_4$ nanocables[133]	Template method (CNFs)–solution method ($CoMn_2O_4$)	~300 nm/N/A	$CoMn_2O_4$, N/A	870 mA h g^{-1} after 150 cycles	200 mA g^{-1}
CNF@SnO_2 nanofibers[123]	Electrospinning (CNFs)–electrodeposition (SnO_2)	250 nm/N/A	SnO_2, 13.3 wt%	540 mA h g^{-1} after 100 cycles	50 mA g^{-1}
Fe_3O_4 anchored CNFs[128]	Biomass method (CNFs)–hydrothermal method (Fe_3O_4)	~30 nm/N/A	Fe_3O_4, 53 wt%	755 mA h g^{-1} after 80 cycles	100 mA g^{-1}
CNFs@CuO[126]	Electrospinning (CNFs)–electrophoretic deposition (SnO_2)	~250 nm/378 m^2 g^{-1}	CuO, 61.8 wt%	772 mA h g^{-1} after 50 cycles	100 mA g^{-1}
Mn_3O_4 anchored CNFs on graphene foam[132]	Chemical vapor deposition (CNFs)–solution method (Mn_3O_4)	100 nm/N/A	Mn_3O_4, N/A	1210 mA h g^{-1} after 50 cycles	100 mA g^{-1}
CNFs@MoS_2 (ref. 129)	Template method (CNFs)–solvothermal method (MoS_2)	100–140 nm/ 176 m^2 g^{-1}	MoS_2, 72 wt%	688 mA h g^{-1} after 300 cycles	1 A g^{-1}
Porous CNFs@MoS_2 (ref. 130)	Electrospinning (CNFs)–solvothermal method (MoS_2)	~700 nm/ 19.95 m^2 g^{-1}	MoS_2, 22.7 wt%	736 mA h g^{-1} after 50 cycles	50 mA g^{-1}
Ge@CNFs[70]	Electrospinning	~230 nm/ 299.15 m^2 g^{-1}	Ge, 48.1 wt%	1420 mA h g^{-1} after 100 cycles	0.15C
Si@CNFs[137]	Electrospinning	200 nm/N/A	Si, 34.7 wt%	1300 mA h g^{-1} after 80 cycles	0.5C
SnO_2@CNFs[138]	Electrospinning	230–280 nm/N/A	SnO_2, 28 wt%	608 mA h g^{-1} after 200 cycles	0.5 Ag^{-1}
Fe_2O_3@CNFs[139]	Electrospinning	487 nm/N/A	Fe_2O_3, 11.33 wt%	488 mA h g^{-1} after 75 cycles	50 mA g^{-1}
CoO@CNFs[140]	Electrospinning	200 nm/N/A	CoO, 29.5 wt%	633 mA h g^{-1} after 52 cycles	100 mA g^{-1}
TiO_2@CNFs[141]	Electrospinning	80–120 nm/N/A	TiO_2, 65.52 wt%	206 mA h g^{-1} after 100 cycles	30 mA g^{-1}
TiO_2(B)@CNFs[142]	Electrospinning	~100 nm/N/A	TiO_2, 36.67 wt%	560 mA h g^{-1} after 100 cycles	30 mA g^{-1}
Si@CNFs–C[135]	Electrospinning (Si@CNFs), CVD (carbon coating layer)	~250 nm/N/A	Si, 10 wt%	700 mA h g^{-1} after 30 cycles	50 mA g^{-1}
Si@C/CNF[143]	Template method (carbon coating layer), electrospinning (CNF)	200–300 nm/N/A	Si, 31 wt%	728 mA h g^{-1} after 40 cycles	50 mA g^{-1}
Sn@porous CNFs[69]	Electrospinning, PMMA template	~2 μm/N/A	Sn, 66 wt%	648 mA h g^{-1} after 140 cycles	0.5C
Sn@C/hollow porous CNFs[144]	Electrospinning, mineral oil template	150–250 nm/N/A	Sn, 66 wt%	737 mA h g^{-1} after 200 cycles	0.5C
Si@porous CNFs[136]	Electrospinning, SiO_2 template	200–500 nm/N/A	Si, 50.2 wt%	1104 mA h g^{-1} after 100 cycles	0.5 A g^{-1}
Si@hollow CNFs[74]	Electrospinning, CVD, SiO_2 template method	~200 nm/N/A	Si, 47 wt%	1000 mA h g^{-1} after 200 cycles	1 A g^{-1}
Co_3O_4@porous CNFs[145]	Electrospinning, PMMA template	100–300 nm/ 33 m^2 g^{-1}	Co_3O_4, 67.7 wt%	932 mA h g^{-1} after 100 cycles	100 mA g^{-1}
CoO@porous CNFs[146]	Electrospinning	400 nm/N/A	CoO, 51 wt%	853.5 mA h g^{-1} after 100 cycles	140 mA g^{-1}

Published on 20 June 2017. Downloaded by University of Western Ontario on 27/07/2017 20:28:34.

Table 3 (*Contd.*)

Materials	Preparation strategy	Diameter & surface area	Active material & weight content	Electrochemical performance	Rate
SnO_x/CNF/CNT[148]	Electrospinning	100–300 nm/N/A	SnO_x, 17 wt%	405 mA h g^{-1} after 300 cycles	2 A g^{-1}
TiO_2@N-doped porous CNFs[149]	Electrospinning	~300 nm/ 191 m^2 g^{-1}	TiO_2, N/A	264 mA h g^{-1} after 100 cycles	33 mA g^{-1}
SnO_2@N-doped CNFs[150]	Electrospinning	~150 nm/ 506 m^2 g^{-1}	SnO_2, 29.6 wt%	754 mA h g^{-1} after 300 cycles	1 A g^{-1}
$Li_4Ti_5O_{12}$/CNF/rGO[151]	Electrospinning	~1 μm/170 m^2 g^{-1}	$Li_4Ti_5O_{12}$, 92.8 wt%	101 mA h g^{-1} after 1300 cycles	22C

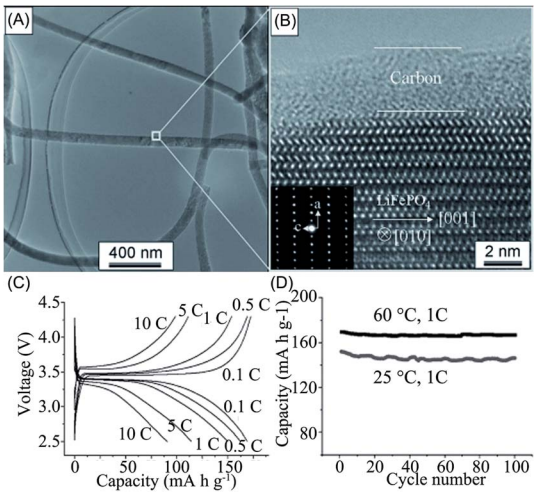

Fig. 13 (A) TEM, (B) HRTEM images, (C) voltage profiles at different current densities from 0.1 to 10C and (D) cycle performance at 1C of carbon coated single crystalline LFP nanowires. Reproduced with permission,[155] Copyright© 2011 Wiley.

As displayed in Table 4, CNFs play a crucial role in the enhancement of the mass and charge transport and protection for the cathode materials as the substrate. Since the cathode materials are facing two main challenges, low ionic and electronic conductivity, the utilization of CNFs cannot only enhance electrical conductivity *via* the formation of a 3D conductive network but also facilitate electron transport through increasing the contact area between the electrode and electrolyte and downsizing the particles of cathode materials. However, CNFs display negligible capacity in the operation window of the cathode materials, decreasing the overall capacity of the composites. The content of CNFs should be adjusted to balance between the beneficial effect on ion & electron transfer and overall capacity. Additionally, the formed 3D network with macropores provides good access to the electrolyte, while the structure would lower the tap density of cathode materials and energy density, which is one crucial factor for practical application. Therefore, the structure and composition of the CNF-based cathode materials should be

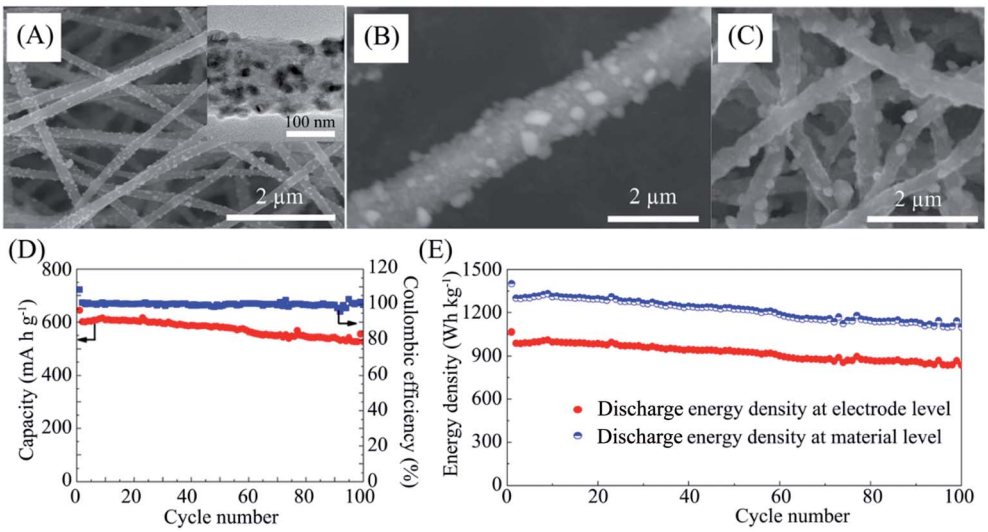

Fig. 14 (A) SEM and TEM images of the FeS_2@carbon fiber; SEM images of the Al_2O_3-coated FeS_2@carbon fiber before cycling (B) and after cycling (C). (D) & (E) Electrochemical performance of the Al_2O_3-coated FeS_2@carbon fiber electrode tested in the solvent-in-salt electrolyte in the voltage range of 1.0–3.0 V (*vs.* Li/Li^+). (D) Capacity retention test and (E) discharge energy density *vs.* cycling number at the material level (~W h kg^{-1}-FeS_2) and the electrode level (~W h kg^{-1}-FeS_2 electrode). Reproduced with permission,[165] Copyright© 2015 American Chemical Society.

Published on 20 June 2017. Downloaded by University of Western Ontario on 27/07/2017 20:28:34.

Table 4 Electrochemical performance of carbon nanofiber-based composites as cathodes for LIBs

Materials	Preparation strategy	Diameter & surface area	Active material & weight content	Electrochemical performance	Rate
$LiFePO_4$@CNFs[155]	Electrospinning	~100 nm/N/A	$LiFePO_4$, 94 wt%	146 mA h g^{-1} after 100 cycles	1C
$LiFePO_4$@CNFs[156]	Electrospinning	250–410 nm/ 167.73 m^2 g^{-1}	$LiFePO_4$, 94.8 wt%	125 mA h g^{-1} after 500 cycles	5C
$LiFePO_4$/CNFs/CNTs[158]	Electrospinning	168 nm/N/A	$LiFePO_4$, 74.8 wt%	169 mA h g^{-1} after 50 cycles	0.05C
Li_2MnSiO_4@CNFs[159]	Electrospinning	180–250 nm/N/A	Li_2MnSiO_4, 80 wt%	247 mA h g^{-1} after 20 cycles	0.05C
$Li_2Mn_{0.8}Fe_{0.2}SiO_4$@CNFs[161]	Electrospinning	160–230 nm/N/A	$Li_2Mn_{0.8}Fe_{0.2}SiO_4$, 80.2 wt%	~140 mA h g^{-1} after 50 cycles	0.05C
$LiNi_{0.5}Mn_{1.5}O_4$/CNFs[162]	Chemical vapor deposition (CNFs), vacuum filtration (composite)	~100 nm, 35–45 m^2 g^{-1}	$LiNi_{0.5}Mn_{1.5}O_4$, 50 wt%	~137 mA h g^{-1} after 500 cycles	0.5C
FeS@graphitic porous CNFs[163]	Electrospinning	~100 nm/226 m^2 g^{-1}	FeS, 70 wt%	450 mA h g^{-1} after 50 cycles	0.5C
Al_2O_3-coated FeS_2@CNFs[165]	Electrospinning (FeS_2@CNFs), ALD (Al_2O_3)	300 nm/N/A	FeS_2, 76.03 wt%	530 mA h g^{-1} after 100 cycles	200 mA g^{-1}

optimized to balance all factors and realize high electrochemical performance for next-generation high-energy commercial lithium-ion batteries.

4. Carbon nanofibers applied in sodium-ion batteries

Due to the low-cost and abundance of resources with promising potential in applications of medium and large-scale energy storage, sodium-ion batteries (NIBs) have gained intensive attention as potential alternatives to lithium-ion batteries.[13] Nevertheless, the Na^+ shows a relatively sluggish intercalation mechanism compared to Li^+ because of the larger ion radius (almost 55% larger than that of Li^+).[15] Therefore, the current research of NIBs mainly focus on the development of advanced electrode materials to gain improved electrochemical performance. Similarly, along with the wide application of CNFs in the electrode materials for the LIBs, CNFs have been intensively studied in the NIBs to enhance electrochemical activity and electrochemical performance. In this section, carbon nanofiber-based anode and cathode materials will be summarized and discussed with a focus on the rational structure designs leading to improved electrochemical performance.

4.1 Carbon nanofiber-based anode materials for sodium-ion batteries

For the current commercial graphite-based anode materials for the LIBs, very low sodium-storage capacity can be delivered, due to the relatively narrow inter-layer distance and weak bonding to sodium.[166–168] Hence, a great range of other anode materials have been intensively studied, such as disordered carbonaceous materials, alloys, metal oxides and metal sulfides. Among the anode materials, CNFs have been widely applied directly as the anodes or as conductive substrates to further improve the electrochemical performance of active materials.[50,78,169]

4.1.1 Carbon nanofiber anode materials for sodium-ion batteries. As discussed above, graphite-based materials are not suitable for sodium storage; however, the sodium storage capabilities of the carbonaceous materials can be improved by creating defect sites.[170] Among the disordered carbonaceous materials, 1D CNFs fabricated from pyrolysis of polymer nanofibers shows highly improved sodium storage capacity, owing to a large number of defect sites to store sodium in addition to improved electronic & ionic conductivity.[23,49,50,78,102,171–179] Luo *et al.*[171] and Chen *et al.*[173] fabricated CNFs *via* carbonization of cellulose nanofibers and electrospun polymer nanofibers, respectively, presenting improved electrochemical performance due to the increased number of defects in the CNFs. To further increase the sodium-storage capacity, Li and co-workers[50] synthesized porous carbon nanofibers (P-CNFs) through an electrospinning method with the triblock copolymer Pluronic F-127 as the template. As displayed in Fig. 15A, P-CNFs show a 3D interconnected structure with plenty of micropores, formed from the decomposition of the F-127 during carbonization, which additionally presents an excellent structure stability during cycling without obvious cracking (Fig. 15B). As a result of structural stability, the P-CNFs display a high reversible capacity of 266 mA h g^{-1} after 100 cycles at a current density of 50 mA g^{-1} and enhanced rate capability of 60 mA h g^{-1} cycled at a high rate of 10 A g^{-1} (Fig. 15C and D). Additionally, similar to the carbonaceous anode materials for the LIBs, heteroatom-doping (mainly nitrogen-doping) and activation methods are viable strategies to produce defects and increase ion-storage sites in carbonaceous materials. Although several studies used high-nitrogen-content polymers as the precursors to form N-doped carbon nanofibers, such as polypyrrole and polyimide,[23,172,174,176] the treatment of carbonaceous materials with nitrogen-containing materials (*e.g.* nitrogen, and urea) is another efficient strategy to realize nitrogen-doping.[177,178] To further promote enhanced sodium-storage performance, nitrogen and oxygen

Published on 20 June 2017. Downloaded by University of Western Ontario on 27/07/2017 20:28:34.

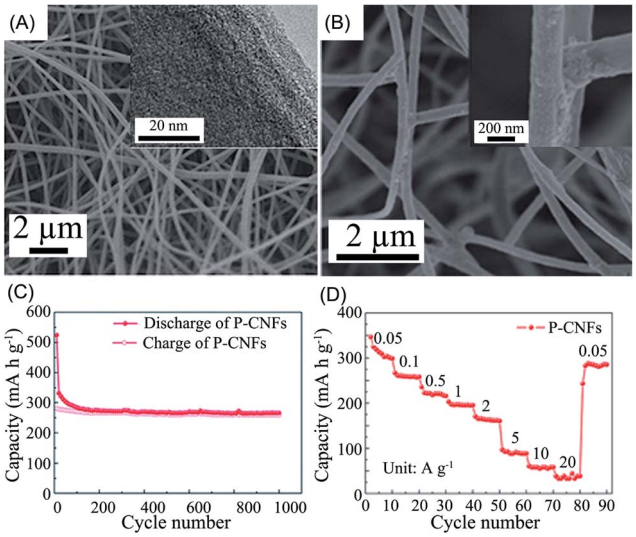

Fig. 15 SEM and TEM images of the P-CNFs before cycling (A) and after cycling (B). (C) & (D) Electrochemical performance for the P-CNFs tested in the voltage range of 0.001–2.0 V (*vs.* Na/Na^+). (C) Cycle performance at the current density of 50 mA g^{-1} and (D) rate performance at different current densities. Reproduced with permission,[50] Copyright© 2014 Royal Society of Chemistry.

dual-doped porous carbon nanofibers (NOC) were prepared by Wang and co-workers[78] *via* carbonization of bacterial cellulose@PANI nanofibers and activation with KOH. As displayed in Fig. 16A and B, the porous carbon nanofibers form a 3D interconnected network, which serves as a fast electron transfer pathway with a concentration of sodium storage sites, and display nitrogen & oxygen dual doping (Fig. 16C and D), which further enhance the electronic conductivity and access to electrolytes. Benefiting from the unique structure, the NOC composite presents a high reversible capacity of 545 mA h g^{-1} after 100 cycles at a current density of 100 mA g^{-1} and improved rate capability (Fig. 16E and F).

As displayed in Table 5, the fabrication of porous structures and heteroatom doping has been demonstrated to be beneficial to the improvement of the sodium storage performance in the CNFs. Similar to CNF anode materials for the LIBs, the number of sodium-ion storage sites in CNFs would determine the electrochemical performance and the porous structure has an important effect on the electron & ion transport, growth of the SEI layer, irreversible capacity and mechanical strength, simultaneously. However, the rational porous structure of CNF anode materials for NIBs should be different from that for LIBs due to the larger ion radius of sodium ion. It is postulated that CNF anodes for NIBs require pores of a larger diameter than those for LIBs. There are few studies focusing on the comparison of rational porous structures for LIBs and NIBs, respectively, including pore size, pore number and hierarchical pores. Further investigations are needed to clarify the challenges.

4.1.2 Carbon nanofibers-based composite anode materials for sodium-ion batteries. Similar to LIBs, the research of the anode materials for NIBs has been extended from carbonaceous materials as discussed above to other anode materials, such as alloys, metal-oxides and metal sulfides/selenides with higher theoretical capacity. For the alloy anode materials, the research is primarily focused on Sb and Sn, since the Si and Ge show sluggish kinetics of sodiation and low sodium storage capacity.[180] Sb and Sn also undergo huge volume change during

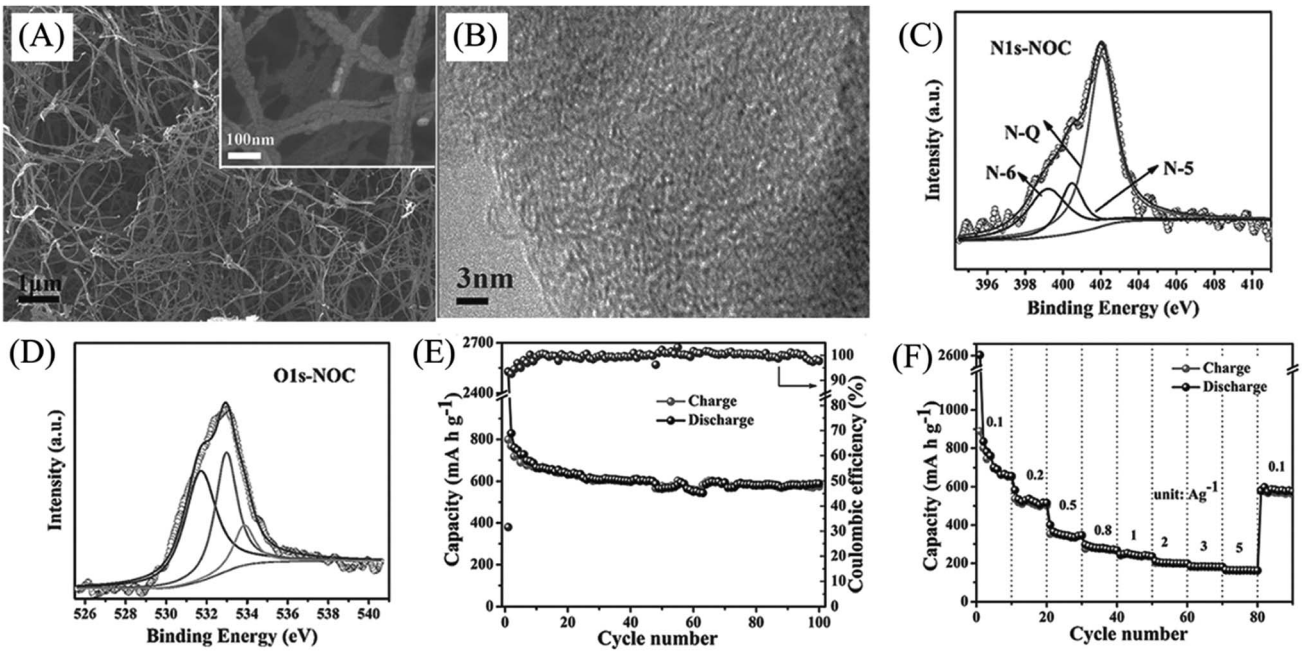

Fig. 16 (A) SEM and (B) HRTEM images of the ONC composite. (C) N1s and (D) O1s XPS spectra of the ONC composite. (E) & (F) Electrochemical performance of the P-CNFs tested in the voltage range of 0.001–2.8 V (*vs.* Na/Na^+). (E) Cycle performance at the current density of 100 mA g^{-1} and (D) rate performance at different current densities. Reproduced with permission,[78] Copyright© 2016 Wiley.

 This journal is © The Royal Society of Chemistry 2017

Published on 20 June 2017. Downloaded by University of Western Ontario on 27/07/2017 20:28:34.

Table 5 Electrochemical performance of carbon nanofibers as anodes for NIBs

Materials	Preparation strategy	Diameter & surface area	Electrochemical performance	Rate
CNFs[171]	Biomass method	50–100 nm/377 $m^2 g^{-1}$	176 mA h g^{-1} after 600 cycles	200 mA g^{-1}
CNFs[173]	Electrospinning	200–300 nm/N/A	233 mA h g^{-1} after 50 cycles	50 mA g^{-1}
Porous CNFs[50]	Electrospinning, F127 template	~280 nm/74.59 $m^2 g^{-1}$	266 mA h g^{-1} after 100 cycles	50 mA g^{-1}
CNFs@N-doped porous carbon[172]	Biomass (CNFs), oxidative template assembly (porous carbon)	80–110 nm/300.2 $m^2 g^{-1}$	240 mA h g^{-1} after 100 cycles	100 mA g^{-1}
N-Doped porous CNFs[23]	Oxidative template assembly	50–70 nm/1508 $m^2 g^{-1}$	243 mA h g^{-1} after 100 cycles	50 mA g^{-1}
N-Doped CNFs[174]	Electrospinning	100–300 nm/564.4 $m^2 g^{-1}$	377 mA h g^{-1} after 100 cycles	100 mA g^{-1}
N-Doped hollow CNFs[176]	Oxidative template assembly, KOH activation	~300 nm/868 $m^2 g^{-1}$	160 mA h g^{-1} after 100 cycles	50 mA g^{-1}
N-Doped CNFs[177]	Electrospinning, N_2 treatment	~150 nm/513.89 $m^2 g^{-1}$	254 mA h g^{-1} after 100 cycles	50 mA g^{-1}
N-Doped CNFs[178]	Electrospinning, urea treatment	~250 nm/8.16 $m^2 g^{-1}$	354 mA h g^{-1} after 100 cycles	50 mA g^{-1}
N,O-Doped porous CNFs[78]	Biomass (CNFs), oxidative template assembly (porous carbon), KOH activation	100–150 nm/1426.1 $m^2 g^{-1}$	545 mA h g^{-1} after 100 cycles	100 mA g^{-1}
N,B-Doped porous CNFs[179]	Biomass (CNFs), $NH_4HB_4O_7 \cdot H_2O$ treatment	30–80 nm/1585 $m^2 g^{-1}$	581 mA h g^{-1} after 120 cycles	100 mA g^{-1}

the sodiation/desodiation process and suffer from rapid capacity degradation, which is also a significant limitation of some metal oxide anode materials.[15] In addition, the sluggish mass and electron transport rate during the sodiation process leads to poor cycle performance. Therefore, the two types of structures based on CNFs applied in LIBs (*i.e.* outer-surface anchoring and encapsulation structures) have also been investigated to further improve the electrochemical performance of NIBs.

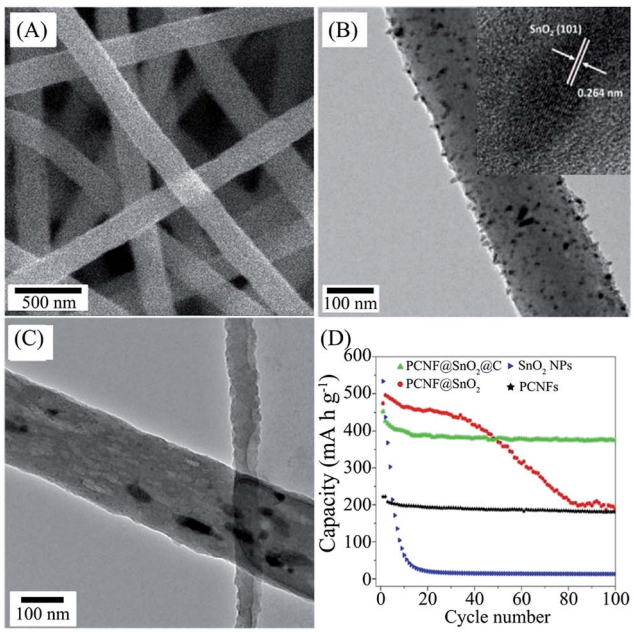

Fig. 17 (A) SEM, (B) TEM & HRTEM images before cycles and (C) TEM image after cycles of the PCNF@SnO_2@C composite. (D) Cycle performance of the PCNF@SnO_2@C composite the current density of 50 mA g^{-1} in the voltage range of 0.01–3.0 V (*vs.* Na/Na^+). Reproduced with permission,[181] Copyright© 2015 American Chemistry Society.

As the CNF-based outer-surface anchoring structure could enhance the electron transport and access to the electrolyte, it is likely that the anode materials anchored to the surface will yield improved sodium storage performance. Hou and co-workers[57] prepared Sb nanoparticles anchored on PPy derived CNFs, showing improved cycling performance and capacity retention of 96.7% after 100 cycles at a current density of 100 mA g^{-1}. To further improve the structural stability and cyclability of the outer-surface anchoring structure, Dirican *et al.*[181] fabricated carbon coating layers on the surface of SnO_2 electrodeposited porous carbon nanofibers (PCNF@SnO_2@C). Fig. 17A and B display the morphology of the PCNF@SnO_2@C composite, consisting of SnO_2 nanoparticles grown on the surface of the electrospun CNFs coated with amorphous carbon layers. Owning to the protection effect of the carbon coating layers and elastic CNFs, the PCNF@SnO_2@C composite presents excellent structure stability during cycling (Fig. 17C) and better cyclability than PCNF@SnO_2 without carbon coating, a high reversible capacity of 374 mA h g^{-1} after 100 cycles at a current density of 50 mA g^{-1} (Fig. 17D).

Compared with the outer-surface anchoring structures, the encapsulation technique has been applied in more studies to improve the electrochemical performance of the non-carbon anode materials. Zhu *et al.*[169] and Wu *et al.*[44] have fabricated Sb nanoparticles embedded in CNFs *via* an electrospinning method to stabilize the Sb, which suffers from the huge volume change during cycling. This type of encapsulation structure based on CNFs has been widely utilized in other alloy-type anode materials to enhance structural stability, such as

Published on 20 June 2017. Downloaded by University of Western Ontario on 27/07/2017 20:28:34.

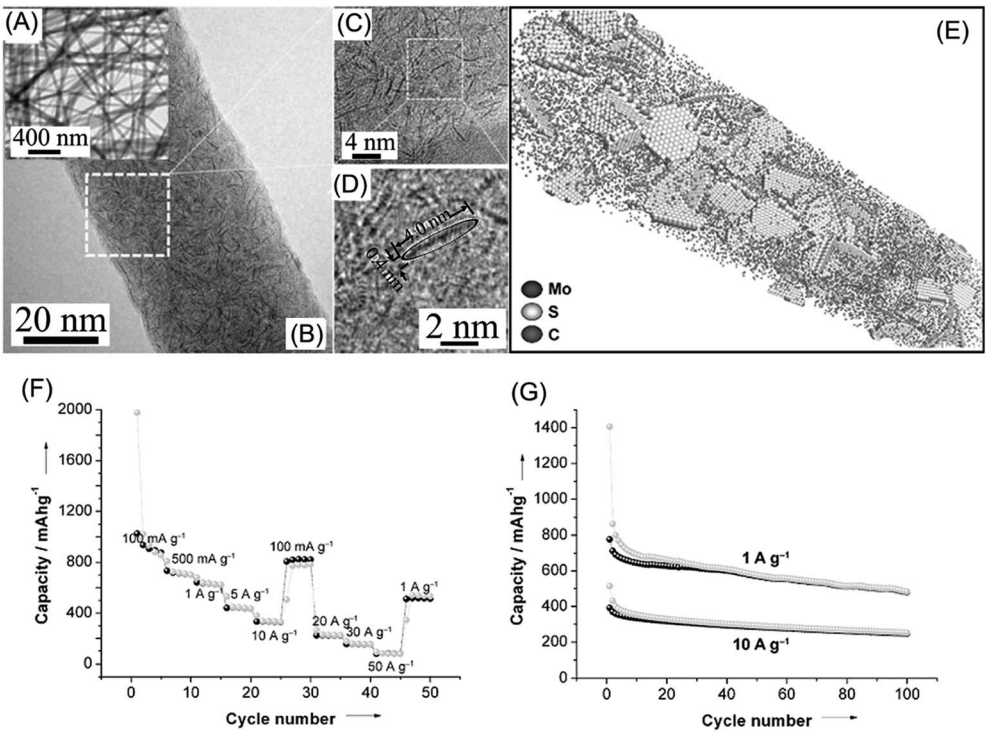

Fig. 18 (A–C) TEM and (D) HRTEM images of single-layered MoS_2 nanoplates embedded in carbon nanofibers; (E) schematic representation based on TEM to demonstrate the unique morphology of the composite nanofibers (F) rate performance and (G) cycle performance of single-layered MoS_2 nanoplates embedded in carbon nanofibers at 1 and 10 A g^{-1} in the voltage range of 0.005–3.0 V (*vs.* Na/Na^+) Reproduced with permission,[47] Copyright 2014, Wiley.

Sn[182,183] and SnSb alloys.[184,185] Furthermore, the metal oxides, metal sulfides and metal selenides such as SnO_2,[148] $Li_4Ti_5O_{12}$,[186] TiO_2,[187] $MnFe_2O_4$,[188] MoS_2,[47,189] $NiSe_2$ (ref. 190) and $FeSe_2$ (ref. 191) have been intensively researched to improve the ionic & electronic conductivity and structure stability *via* fabricating the encapsulation structures. The size of the anode materials in CNFs has a significant effect on the electrochemical activity. To realize high electrochemical activity, Zhu and co-workers[47] prepared single-layered MoS_2 nanoplates (0.4 nm in thickness) embedded in the CNFs *via* the electrospinning method as displayed in Fig. 18A–D. Benefiting from the unique structure, the single-layered MoS_2 carbon nanofiber composite presents excellent rate and cycling performance of high reversible capacities of 484 and 253 mA h g^{-1} after 100 cycles at a current density of 1 and 10 A g^{-1}, respectively (Fig. 18F and G), showcasing the high electrochemical activity of the composite.

As presented in Table 6, the non-carbon anode materials suffering from large volume variation or sluggish mass and charge transport have been intensively studied *via* introducing CNFs to fabricate the CNF-based composites through the two main structures (*i.e.* outer-surface anchoring and encapsulation structures) and improve the sodium storage performance. Similar to anode materials for CNF-based anodes for the LIBs, CNFs are able to stabilize the structure, enhance electronic and ionic transport. Nevertheless, the volume change of anode materials for the NIBs is more serious than that of the same anodes for LIBs owing to the larger sodium ion. The accommodation effect of CNFs on the anodes for NIBs should be further clarified, focusing on the study of the influence of weight content and morphology (*e.g.* thickness, diameter, porous structure). On the other hand, different from the CNF-based anode materials, the sodium-ion diffusion in the CNF substrate should be further considered, due to the larger diameter and low bonding effect of the sodium ion. Furthermore, the high surface area and low sodium storage capacity of CNFs can result in irreversible capacity and reduction of overall capacity. The weight content of CNFs and structural design of the composite anode materials should be adjusted to lower the negative effect. Therefore, further study is required to consider the combined effect of CNFs on the non-carbon anode materials for NIBs.

4.2 Carbon nanofiber-based composite cathode materials for the sodium-ion batteries

In the case of cathodes, numerous materials with similar crystalline structures to those of which are found in LIBs have been exhaustively studied, such as manganese oxides (*e.g.* $Na_{0.44}MnO_2$ and λ-MnO_2),[192,193] layered oxides (*e.g.* P2-Na_x-CoO_2),[194] natrium super ion conductor (NASICON)-type materials (*e.g.* $Na_3V_2(PO_4)_3$),[195] and olivines (*e.g.* $FePO_4$ and $Na(Fe_{0.5}Mn_{0.5})FePO_4$).[196,197] For these cathode materials, CNFs have been demonstrated to be good conductive additives and improve the electronic conductivity and sodium-storage performance.[45,198]

Among the cathode materials, the NASICION-type materials (*e.g.* N $Na_3V_2(PO_4)_3$) have been demonstrated to be promising cathodes for NIBs. However, the electrochemical performance

 This journal is © The Royal Society of Chemistry 2017

Published on 20 June 2017. Downloaded by University of Western Ontario on 27/07/2017 20:28:34.

Table 6 Electrochemical performance of carbon nanofiber-based composites as anodes for NIBs

Materials	Preparation strategy	Diameter & surface area	Active material & weight content	Electrochemical performance	Rate
Sb anchored on CNFs[57]	Biomass method (CNFs), solution method (Sb)	~50 nm/160.3 m^2 g^{-1}	Sb, 80.8 wt%	542.5 mA h g^{-1} after 100 cycles	100 mA g^{-1}
PCNF@SnO_2@C[181]	Electrospinning (CNFs), electrodeposition (SnO_2), CVD (carbon coating layer)	~200 nm/N/A	SnO_2, 38.5 wt%	374 mA h g^{-1} after 100 cycles	50 mA g^{-1}
Sb@CNFs[44]	Electrospinning	~200 nm/N/A	Sb, 38 wt%	446 mA h g^{-1} after 400 cycles	200 mA g^{-1}
Sb@CNFs[169]	Electrospinning	~250 nm/N/A	Sb, 54 wt%	350 mA h g^{-1} after 300 cycles	100 mA g^{-1}
Sn nanodots@porous N-doped CNFs[183]	Electrospinning	120 nm/316 m^2 g^{-1}	Sn, 63 wt%	483 mA h g^{-1} after 1300 cycles	2 A g^{-1}
SnSb@porous CNFs[184]	Electrospinning	~250 nm/N/A	SnSb, 60 wt%	345 mA h g^{-1} after 200 cycles	0.2C
SnSb@porous CNFs[185]	Electrospinning	100 nm/N/A	SnSb, 44 wt%	600 mA h g^{-1} after 100 cycles	200 mA g^{-1}
SnO_x@CNFs[148]	Electrospinning	100–300 nm/N/A	SnO_x, 17 wt%	210 mA h g^{-1} after 300 cycles	500 mA g^{-1}
$Li_4Ti_5O_{12}$@CNFs[186]	Electrospinning	100 nm/N/A	$Li_4Ti_5O_{12}$, 90.5 wt%	162.5 mA h g^{-1} after 100 cycles	0.2C
TiO_2@CNFs[187]	Electrospinning	~120 nm/15.7 m^2 g^{-1}	TiO_2, 81 wt%	237.1 mA h g^{-1} after 1000 cycles	200 mA g^{-1}
$MnFe_2O_4$@CNFs[188]	Electrospinning	180 nm/239.6 m^2 g^{-1}	$MnFe_2O_4$, 66.8 wt%	360 mA h g^{-1} after 4200 cycles	2000 mA g^{-1}
MoS_2@CNFs[189]	Electrospinning	~150 nm/N/A	MoS_2, 83.2 wt%	283.9 mA h g^{-1} after 600 cycles	100 mA g^{-1}
MoS_2@CNFs[47]	Electrospinning	~50 nm/N/A	MoS_2, 62 wt%	484 mA h g^{-1} after 100 cycles	1 A g^{-1}
$NiSe_2$–rGO–CNFs[190]	Electrospinning, selenization	~1 μm/119 m^2 g^{-1}	$NiSe_2$, 75 wt%	468 mA h g^{-1} after 100 cycles	200 mA g^{-1}
Hollow nanospheres $FeSe_2$–rGO–graphitic CNFs[191]	Electrospinning, selenization	~2 μm/34 m^2 g^{-1}	$FeSe_2$, 73 wt%	412 mA h g^{-1} after 150 cycles	1 A g^{-1}

of $Na_3V_2(PO_4)_3$ (NVP) is limited due to the high electrical resistance. Based on the above discussion, it is rational to downsize the particles and fabricate an electronically conductive material–NVP composite to enhance the electrochemical activity. The fabrication of NVP–CNFs composites has proven to be an efficient strategy to overcome the limitations of NVP.[45,198,199] Liu and co-workers[45] synthesized NVP nanoparticles encapsulated in the CNFs (NVP/C) *via* the electrospinning method. As presented in Fig. 19A and B, the NVP nanoparticles are embedded in the CNFs, forming the interconnected structure. Due to its unique structure, the NVP–C composite showed a high reversible capacity of 117 mA h g^{-1} after 50 cycles and a current density of 0.1C and retained improved rate capacities at higher current densities (Fig. 19C and D).

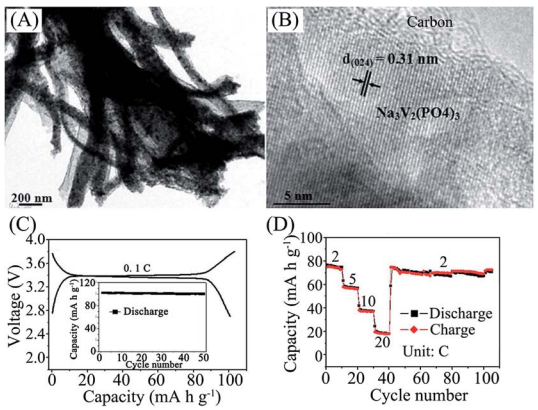

Fig. 19 (A) TEM and (B) HRTEM images of the hierarchical $Na_3V_2(PO_4)_3$/C composite; (C) cycle performance at 0.1C and (D) rate performance of the $Na_3V_2(PO_4)_3$/C composite at different current densities in the voltage range of 2.6–4.1 V (*vs.* Na/Na^+). Reproduced with permission,[45] Copyright 2014, Royal Society of Chemistry.

Similar to the cathode materials for the LIBs, the cathodes for the NIBs also require enhancement of electron and ion transport to improve the slow kinetics of sodium-ion storage. The formed 3D conductive network provides good electron transport paths and good access for the electrolyte, finally improving the electrochemical performance of the cathode materials. However, the negligible capacity of the CNFs in the operation window of the cathode materials decrease the overall capacity of composite cathode materials. Therefore, the weight content of the CNFs should be adjusted to balance the enhancement effect of electron & ion transport and overall capacity of the composite cathodes. In addition, the diffusion of sodium ions in the CNFs is different from that of lithium ions, which should be further studied to clarify the effect of the CNFs on the cathodes for the NIBs.

5. Conclusions and perspective

In this review, we have summarized the progress of the application of carbon nanofibers in LIBs and NIBs, including the introduction of the preparation strategies of CNFs and efficient utilization in the development of advanced electrode materials. Furthermore, this review focuses on the evolution in structures and composition of CNF-based electrode materials for LIBs and NIBs and the resulting improvement in electrochemical performance. We have placed an emphasis on the discussion of

Published on 20 June 2017. Downloaded by University of Western Ontario on 27/07/2017 20:28:34.

the influence of structural morphology on the stability during cycling, transport rate of the electrons and ions, electrochemical activity and electrochemical performance. CNFs have been demonstrated to be superior anode materials for LIBs and NIBs in addition to acting as effective substrates for other non-carbon anode & cathode materials. The composite electrodes improve electrochemical performance, due to several advantages including: (a) convenience of fabrication *via* various strategies, such as porous structures, such as outer surface anchoring structures and encapsulation structures, which enhance active sites and structure stability; (b) 3D interconnected networks to facilitate charge transfer along the fast electronic transport pathways and ensure good access to the electrolytes; (c) a high surface area–volume ratio to decrease the distance of the mass transport, further enhancing ionic transfer kinetics.

Currently, CNFs show great promise in the application of next-generation high-energy LIBs and NIBs through rational structural designs. Nevertheless, there remain several challenges to overcome in the future before practical applications are realized. Firstly, the influence of CNFs on the lithium- & sodium-storage performance with different structures and compositions should be further studied to figure out the most efficient structure designs for different electrode materials. Secondly, the improvement of ionic and electronic conductivity *via* the introduction of CNFs should be further researched to understand the mechanism and its effects on the electrochemical performance. Finally, large-scale fabrication strategies for the CNF-based electrode materials are urgently required to meet the demand for their practical applications. In industrial scale production, the main concerns are the preparation rate and cost. The electrospinning method has undergone rapid development to realize industrial scale production methods *via* multi-spinnerets of non-needle systems, while the biomass method is another potential strategy to obtain large amounts of precursors for the CNFs, as the bacterial cellulose is commercially available with an acceptable production rate. Along with the continuously increased production rate and decreased cost, the development of CNF-based nanostructures would hold great promise to realize the next-generation of high-energy lithium-ion & sodium-ion batteries in the not-too-distant future.

Acknowledgements

This work was financially supported by the National Key Research Program (No. 2016YFB0100305), the National Natural Science Foundation of China (Grant No. 51622210 and 21373195), the Fundamental Research Funds for the Central Universities (WK3430000004), and the Collaborative Innovation Center of Suzhou Nano Science and Technology.

References

1 M. I. Hoffert, K. Caldeira, G. Benford, D. R. Criswell, C. Green, H. Herzog, A. K. Jain, H. S. Kheshgi, K. S. Lackner and J. S. Lewis, *Science*, 2002, **298**, 981–987.
2 G. J. Herbert, S. Iniyan, E. Sreevalsan and S. Rajapandian, *Renewable Sustainable Energy Rev.*, 2007, **11**, 1117–1145.
3 J. B. Goodenough, *Acc. Chem. Res.*, 2012, **46**, 1053–1061.
4 K. Solangi, M. Islam, R. Saidur, N. Rahim and H. Fayaz, *Renewable Sustainable Energy Rev.*, 2011, **15**, 2149–2163.
5 N. Panwar, S. Kaushik and S. Kothari, *Renewable Sustainable Energy Rev.*, 2011, **15**, 1513–1524.
6 H. Lund and B. V. Mathiesen, *Energy*, 2009, **34**, 524–531.
7 Z. Yang, J. Zhang, M. C. Kintner-Meyer, X. Lu, D. Choi, J. P. Lemmon and J. Liu, *Chem. Rev.*, 2011, **111**, 3577–3613.
8 A. Barré, B. Deguilhem, S. Grolleau, M. Gérard, F. Suard and D. Riu, *J. Power Sources*, 2013, **241**, 680–689.
9 H.-C. Yu, C. Ling, J. Bhattacharya, J. C. Thomas, K. Thornton and A. Van der Ven, *Energy Environ. Sci.*, 2014, **7**, 1760–1768.
10 B. Scrosati and J. Garche, *J. Power Sources*, 2010, **195**, 2419–2430.
11 A. Yoshino, *Angew. Chem., Int. Ed.*, 2012, **51**, 5798–5800.
12 S. Manzetti and F. Mariasiu, *Renewable Sustainable Energy Rev.*, 2015, **51**, 1004–1012.
13 B. L. Ellis and L. F. Nazar, *Curr. Opin. Solid State Mater. Sci.*, 2012, **16**, 168–177.
14 H. Pan, Y.-S. Hu and L. Chen, *Energy Environ. Sci.*, 2013, **6**, 2338–2360.
15 M. D. Slater, D. Kim, E. Lee and C. S. Johnson, *Adv. Funct. Mater.*, 2013, **23**, 947–958.
16 L. Weihan, Z. Linchao, W. Ying and Y. Yan, *Sci. China Mater.*, 2016, **59**, 287–321.
17 R. Marom, S. F. Amalraj, N. Leifer, D. Jacob and D. Aurbach, *J. Mater. Chem.*, 2011, **21**, 9938–9954.
18 S. W. Kim, D. H. Seo, X. Ma, G. Ceder and K. Kang, *Adv. Energy Mater.*, 2012, **2**, 710–721.
19 Q. Zhang, E. Uchaker, S. L. Candelaria and G. Cao, *Chem. Soc. Rev.*, 2013, **42**, 3127–3171.
20 M. H. Han, E. Gonzalo, G. Singh and T. Rojo, *Energy Environ. Sci.*, 2015, **8**, 81–102.
21 E. Irisarri, A. Ponrouch and M. Palacin, *J. Electrochem. Soc.*, 2015, **162**, A2476–A2482.
22 Z.-S. Wu, W. Ren, L. Xu, F. Li and H.-M. Cheng, *ACS Nano*, 2011, **5**, 5463–5471.
23 L. Fu, K. Tang, K. Song, P. A. van Aken, Y. Yu and J. Maier, *Nanoscale*, 2014, **6**, 1384–1389.
24 Y. Yang, X. Ji, M. Jing, H. Hou, Y. Zhu, L. Fang, X. Yang, Q. Chen and C. E. Banks, *J. Mater. Chem. A*, 2015, **3**, 5648–5655.
25 C. Chen, J. Liu, M. Stoll, G. Henriksen, D. Vissers and K. Amine, *J. Power Sources*, 2004, **128**, 278–285.
26 T. Song, J. Xia, J.-H. Lee, D. H. Lee, M.-S. Kwon, J.-M. Choi, J. Wu, S. K. Doo, H. Chang and W. I. Park, *Nano Lett.*, 2010, **10**, 1710–1716.
27 C. K. Chan, X. F. Zhang and Y. Cui, *Nano Lett.*, 2008, **8**, 307–309.
28 W. Li, Z. Yang, M. Li, Y. Jiang, X. Wei, X. Zhong, L. Gu and Y. Yu, *Nano Lett.*, 2016, **16**, 1546–1553.
29 B. Pei, H. Yao, W. Zhang and Z. Yang, *J. Power Sources*, 2012, **220**, 317–323.

 This journal is © The Royal Society of Chemistry 2017

Published on 20 June 2017. Downloaded by University of Western Ontario on 27/07/2017 20:28:34.

30 Y. Yu, L. Gu, X. Lang, C. Zhu, T. Fujita, M. Chen and J. Maier, *Adv. Mater.*, 2011, **23**, 2443–2447.
31 L.-H. Hu, F.-Y. Wu, C.-T. Lin, A. N. Khlobystov and L.-J. Li, *Nat. Commun.*, 2013, **4**, 1687.
32 G. Kucinskis, G. Bajars and J. Kleperis, *J. Power Sources*, 2013, **240**, 66–79.
33 Y. Liu, Y. Xu, X. Han, C. Pellegrinelli, Y. Zhu, H. Zhu, J. Wan, A. C. Chung, O. Vaaland and C. Wang, *Nano Lett.*, 2012, **12**, 5664–5668.
34 J. Jiang, Y. Li, J. Liu and X. Huang, *Nanoscale*, 2011, **3**, 45–58.
35 D. Chao, X. Xia, J. Liu, Z. Fan, C. F. Ng, J. Lin, H. Zhang, Z. X. Shen and H. J. Fan, *Adv. Mater.*, 2014, **26**, 5794–5800.
36 H. Wang, L.-F. Cui, Y. Yang, H. Sanchez Casalongue, J. T. Robinson, Y. Liang, Y. Cui and H. Dai, *J. Am. Chem. Soc.*, 2010, **132**, 13978–13980.
37 G. Zhou, D.-W. Wang, F. Li, L. Zhang, N. Li, Z.-S. Wu, L. Wen, G. Q. Lu and H.-M. Cheng, *Chem. Mater.*, 2010, **22**, 5306–5313.
38 B. Qu, C. Ma, G. Ji, C. Xu, J. Xu, Y. S. Meng, T. Wang and J. Y. Lee, *Adv. Mater.*, 2014, **26**, 3854–3859.
39 Y.-X. Wang, Y.-G. Lim, M.-S. Park, S.-L. Chou, J. H. Kim, H.-K. Liu, S.-X. Dou and Y.-J. Kim, *J. Mater. Chem. A*, 2014, **2**, 529–534.
40 A. L. M. Reddy, M. M. Shaijumon, S. R. Gowda and P. M. Ajayan, *Nano Lett.*, 2009, **9**, 1002–1006.
41 X. Li, F. Kang, X. Bai and W. Shen, *Electrochem. Commun.*, 2007, **9**, 663–666.
42 W.-J. Li, S.-L. Chou, J.-Z. Wang, H.-K. Liu and S.-X. Dou, *Nano Lett.*, 2013, **13**, 5480–5484.
43 X. L. Wu, Y. G. Guo, J. Su, J. W. Xiong, Y. L. Zhang and L. J. Wan, *Adv. Energy Mater.*, 2013, **3**, 1155–1160.
44 L. Wu, X. Hu, J. Qian, F. Pei, F. Wu, R. Mao, X. Ai, H. Yang and Y. Cao, *Energy Environ. Sci.*, 2014, **7**, 323–328.
45 J. Liu, K. Tang, K. Song, P. A. van Aken, Y. Yu and J. Maier, *Nanoscale*, 2014, **6**, 5081–5086.
46 L.-F. Cui, Y. Yang, C.-M. Hsu and Y. Cui, *Nano Lett.*, 2009, **9**, 3370–3374.
47 C. Zhu, X. Mu, P. A. van Aken, Y. Yu and J. Maier, *Angew. Chem., Int. Ed.*, 2014, **53**, 2152–2156.
48 L. Qie, W. M. Chen, Z. H. Wang, Q. G. Shao, X. Li, L. X. Yuan, X. L. Hu, W. X. Zhang and Y. H. Huang, *Adv. Mater.*, 2012, **24**, 2047–2050.
49 Y. Cao, L. Xiao, M. L. Sushko, W. Wang, B. Schwenzer, J. Xiao, Z. Nie, L. V. Saraf, Z. Yang and J. Liu, *Nano Lett.*, 2012, **12**, 3783–3787.
50 W. Li, L. Zeng, Z. Yang, L. Gu, J. Wang, X. Liu, J. Cheng and Y. Yu, *Nanoscale*, 2014, **6**, 693–698.
51 J. Liu, K. Song, C. Zhu, C.-C. Chen, P. A. van Aken, J. Maier and Y. Yu, *ACS Nano*, 2014, **8**, 7051–7059.
52 R. H. Baughman, A. A. Zakhidov and W. A. de Heer, *science*, 2002, **297**, 787–792.
53 N. M. Rodriguez, *J. Mater. Res.*, 1993, **8**, 3233–3250.
54 M. Inagaki, Y. Yang and F. Kang, *Adv. Mater.*, 2012, **24**, 2547–2566.
55 Z.-J. Fan, J. Yan, T. Wei, G.-Q. Ning, L.-J. Zhi, J.-C. Liu, D.-X. Cao, G.-L. Wang and F. Wei, *ACS Nano*, 2011, **5**, 2787–2794.
56 X.-Q. Zhang, Q. Sun, W. Dong, D. Li, A.-H. Lu, J.-Q. Mu and W.-C. Li, *J. Mater. Chem. A*, 2013, **1**, 9449–9455.
57 H. Hou, M. Jing, Y. Yang, Y. Zhang, W. Song, X. Yang, J. Chen, Q. Chen and X. Ji, *J. Power Sources*, 2015, **284**, 227–235.
58 G. Zheng, Q. Zhang, J. J. Cha, Y. Yang, W. Li, Z. W. Seh and Y. Cui, *Nano Lett.*, 2013, **13**, 1265–1270.
59 Y. Yao and F. Wu, *Nano Energy*, 2015, **17**, 91–103.
60 K. P. De Jong and J. W. Geus, *Catal. Rev.*, 2000, **42**, 481–510.
61 L. Feng, N. Xie and J. Zhong, *Materials*, 2014, **7**, 3919–3945.
62 R. Zheng, Y. Zhao, H. Liu, C. Liang and G. Cheng, *Carbon*, 2006, **44**, 742–746.
63 H. Terrones, T. Hayashi, M. Munoz-Navia, M. Terrones, Y. Kim, N. Grobert, R. Kamalakaran, J. Dorantes-Davila, R. Escudero and M. Dresselhaus, *Chem. Phys. Lett.*, 2001, **343**, 241–250.
64 M. Endo, Y. A. Kim, M. Ezaka, K. Osada, T. Yanagisawa, T. Hayashi, M. Terrones and M. S. Dresselhaus, *Nano Lett.*, 2003, **3**, 723–726.
65 D. Li and Y. Xia, *Adv. Mater.*, 2004, **16**, 1151–1170.
66 H.-G. Wang, S. Yuan, D.-L. Ma, X.-B. Zhang and J.-M. Yan, *Energy Environ. Sci.*, 2015, **8**, 1660–1681.
67 A. L. Yarin, S. Koombhongse and D. H. Reneker, *J. Appl. Phys.*, 2001, **90**, 4836–4846.
68 A. Greiner and J. H. Wendorff, *Angew. Chem., Int. Ed.*, 2007, **46**, 5670–5703.
69 Y. Yu, L. Gu, C. Zhu, P. A. Van Aken and J. Maier, *J. Am. Chem. Soc.*, 2009, **131**, 15984–15985.
70 W. Li, Z. Yang, J. Cheng, X. Zhong, L. Gu and Y. Yu, *Nanoscale*, 2014, **6**, 4532–4537.
71 Z. Liu, X. Zhang, S. Poyraz, S. P. Surwade and S. K. Manohar, *J. Am. Chem. Soc.*, 2010, **132**, 13158–13159.
72 J. Tu, L. Zhu, K. Hou and S. Guo, *Carbon*, 2003, **41**, 1257–1263.
73 G. Zheng, Y. Yang, J. J. Cha, S. S. Hong and Y. Cui, *Nano Lett.*, 2011, **11**, 4462–4467.
74 H. Wu, G. Zheng, N. Liu, T. J. Carney, Y. Yang and Y. Cui, *Nano Lett.*, 2012, **12**, 904–909.
75 Z. Wang, L. Qie, L. Yuan, W. Zhang, X. Hu and Y. Huang, *Carbon*, 2013, **55**, 328–334.
76 B. Wang, X. Li, B. Luo, J. Yang, X. Wang, Q. Song, S. Chen and L. Zhi, *Small*, 2013, **9**, 2399–2404.
77 W. Wang, Y. Sun, B. Liu, S. Wang and M. Cao, *Carbon*, 2015, **91**, 56–65.
78 M. Wang, Z. Yang, W. Li, L. Gu and Y. Yu, *Small*, 2016, **12**, 2559–2566.
79 Z. Y. Wu, C. Li, H. W. Liang, J. F. Chen and S. H. Yu, *Angew. Chem.*, 2013, **125**, 2997–3001.
80 M. Endo, Y. Kim, T. Hayashi, K. Nishimura, T. Matusita, K. Miyashita and M. Dresselhaus, *Carbon*, 2001, **39**, 1287–1297.
81 B. Zhang, F. Kang, J.-M. Tarascon and J.-K. Kim, *Prog. Mater. Sci.*, 2016, **76**, 319–380.

Published on 20 June 2017. Downloaded by University of Western Ontario on 27/07/2017 20:28:34.

82 X. Mao, T. A. Hatton and G. C. Rutledge, *Curr. Org. Chem.*, 2013, **17**, 1390–1401.
83 F. Agend, N. Naderi and R. Fareghi-Alamdari, *J. Appl. Polym. Sci.*, 2007, **106**, 255–259.
84 C. Kim, K. S. Yang, M. Kojima, K. Yoshida, Y. J. Kim, Y. A. Kim and M. Endo, *Adv. Funct. Mater.*, 2006, **16**, 2393–2397.
85 M. K. Smith, V. Singh, K. Kalaitzidou and B. A. Cola, *ACS Appl. Mater. Interfaces*, 2016, **8**, 14788–14794.
86 H.-W. Liang, Q.-F. Guan, L.-T. Song, H.-B. Yao, X. Lei and S.-H. Yu, *NPG Asia Mater.*, 2012, **4**, e19.
87 P. Roy and S. K. Srivastava, *J. Mater. Chem. A*, 2015, **3**, 2454–2484.
88 V. Etacheri, R. Marom, R. Elazari, G. Salitra and D. Aurbach, *Energy Environ. Sci.*, 2011, **4**, 3243–3262.
89 J.-W. Jung, C.-L. Lee, S. Yu and I.-D. Kim, *J. Mater. Chem. A*, 2016, **4**, 703–750.
90 V. A. Agubra, L. Zuniga, D. Flores, J. Villareal and M. Alcoutlabi, *Electrochim. Acta*, 2016, **192**, 529–550.
91 Z. Shu, R. McMillan and J. Murray, *J. Electrochem. Soc.*, 1993, **140**, 922–927.
92 K. Persson, V. A. Sethuraman, L. J. Hardwick, Y. Hinuma, Y. S. Meng, A. van der Ven, V. Srinivasan, R. Kostecki and G. Ceder, *J. Phys. Chem. Lett.*, 2010, **1**, 1176–1180.
93 Y.-P. Wu, E. Rahm and R. Holze, *J. Power Sources*, 2003, **114**, 228–236.
94 W.-J. Zhang, *J. Power Sources*, 2011, **196**, 13–24.
95 X. L. Wu, Y. G. Guo and L. J. Wan, *Chem.–Asian J.*, 2013, **8**, 1948–1958.
96 P. Poizot, S. Laruelle, S. Grugeon, L. Dupont and J. Tarascon, *Nature*, 2000, **407**, 496–499.
97 L. Ji, Z. Lin, M. Alcoutlabi and X. Zhang, *Energy Environ. Sci.*, 2011, **4**, 2682–2699.
98 W. Li, X. Sun and Y. Yu, *Small Methods*, 2017, **1**, 1600037.
99 W. Li, M. Li, M. Wang, L. Zeng and Y. Yu, *Nano Energy*, 2015, **13**, 693–701.
100 S. A. Klankowski, R. A. Rojeski, B. A. Cruden, J. Liu, J. Wu and J. Li, *J. Mater. Chem. A*, 2013, **1**, 1055–1064.
101 G. Zou, D. Zhang, C. Dong, H. Li, K. Xiong, L. Fei and Y. Qian, *Carbon*, 2006, **44**, 828–832.
102 D. Nan, Z.-H. Huang, R. Lv, L. Yang, J.-G. Wang, W. Shen, Y. Lin, X. Yu, L. Ye and H. Sun, *J. Mater. Chem. A*, 2014, **2**, 19678–19684.
103 X.-B. Cheng, Q. Zhang, H.-F. Wang, G.-L. Tian, J.-Q. Huang, H.-J. Peng, M.-Q. Zhao and F. Wei, *Catal. Today*, 2015, **249**, 244–251.
104 S.-X. Wang, L. Yang, L. P. Stubbs, X. Li and C. He, *ACS Appl. Mater. Interfaces*, 2013, **5**, 12275–12282.
105 D. Nan, J.-G. Wang, Z.-H. Huang, L. Wang, W. Shen and F. Kang, *Electrochem. Commun.*, 2013, **34**, 52–55.
106 D. Deng and J. Y. Lee, *Chem. Mater.*, 2007, **19**, 4198–4204.
107 V. Subramanian, H. Zhu and B. Wei, *J. Phys. Chem. B*, 2006, **110**, 7178–7183.
108 L. Ji, Z. Lin, A. J. Medford and X. Zhang, *Carbon*, 2009, **47**, 3346–3354.
109 L. Ji and X. Zhang, *Electrochem. Commun.*, 2009, **11**, 684–687.
110 L. Ji, M. Rao, S. Aloni, L. Wang, E. J. Cairns and Y. Zhang, *Energy Environ. Sci.*, 2011, **4**, 5053–5059.
111 L. Ji and X. Zhang, *Nanotechnology*, 2009, **20**, 155705.
112 Z. Wang, X. Xiong, L. Qie and Y. Huang, *Electrochim. Acta*, 2013, **106**, 320–326.
113 S. Jun, S. H. Joo, R. Ryoo, M. Kruk, M. Jaroniec, Z. Liu, T. Ohsuna and O. Terasaki, *J. Am. Chem. Soc.*, 2000, **122**, 10712–10713.
114 C. Vix-Guterl, S. Boulard, J. Parmentier, J. Werckmann and J. Patarin, *Chem. Lett.*, 2002, **31**, 1062–1063.
115 Y. Zhu, S. Murali, M. D. Stoller, K. Ganesh, W. Cai, P. J. Ferreira, A. Pirkle, R. M. Wallace, K. A. Cychosz and M. Thommes, *Science*, 2011, **332**, 1537–1541.
116 Y. Chen, Z. Lu, L. Zhou, Y.-W. Mai and H. Huang, *Nanoscale*, 2012, **4**, 6800–6805.
117 Y. Chen, Z. Lu, L. Zhou, Y.-W. Mai and H. Huang, *Energy Environ. Sci.*, 2012, **5**, 7898–7902.
118 Y. Chen, X. Li, X. Zhou, H. Yao, H. Huang, Y.-W. Mai and L. Zhou, *Energy Environ. Sci.*, 2014, **7**, 2689–2696.
119 B. Zhang, Z.-L. Xu, Y.-B. He, S. Abouali, M. A. Garakani, E. K. Heidari, F. Kang and J.-K. Kim, *Nano Energy*, 2014, **4**, 88–96.
120 Y. Chen, X. Li, K. Park, J. Song, J. Hong, L. Zhou, Y.-W. Mai, H. Huang and J. B. Goodenough, *J. Am. Chem. Soc.*, 2013, **135**, 16280–16283.
121 M. Reddy, G. Subba Rao and B. Chowdari, *Chem. Rev.*, 2013, **113**, 5364–5457.
122 S. Goriparti, E. Miele, F. De Angelis, E. Di Fabrizio, R. P. Zaccaria and C. Capiglia, *J. Power Sources*, 2014, **257**, 421–443.
123 L. Ji, Z. Lin, B. Guo, A. J. Medford and X. Zhang, *Chem.–Eur. J.*, 2010, **16**, 11543–11548.
124 Y. Park, M. Oh, J. S. Park, S.-H. Baek, M. Kim, S. Kim and J. H. Kim, *Carbon*, 2015, **94**, 9–17.
125 Z. Lin, L. Ji, M. D. Woodroof and X. Zhang, *J. Power Sources*, 2010, **195**, 5025–5031.
126 S.-H. Park and W.-J. Lee, *Sci. Rep.*, 2015, **5**, 9754.
127 W. Li, M. Li, Z. Yang, J. Xu, X. Zhong, J. Wang, L. Zeng, X. Liu, Y. Jiang and X. Wei, *Small*, 2015, **11**, 2762–2767.
128 Y. Wan, Z. Yang, G. Xiong, R. Guo, Z. Liu and H. Luo, *J. Power Sources*, 2015, **294**, 414–419.
129 F. Zhou, S. Xin, H. W. Liang, L. T. Song and S. H. Yu, *Angew. Chem., Int. Ed.*, 2014, **53**, 11552–11556.
130 Y.-E. Miao, Y. Huang, L. Zhang, W. Fan, F. Lai and T. Liu, *Nanoscale*, 2015, **7**, 11093–11101.
131 H. Mi, Y. Xu, W. Shi, H. Yoo, S. Park, Y. Park and S. M. Oh, *J. Mater. Chem.*, 2011, **21**, 19302–19309.
132 H. Yue, F. Li, Z. Yang, X. Li, S. Lin and D. He, *J. Mater. Chem. A*, 2014, **2**, 17352–17358.
133 G. Zhang, H. B. Wu, H. E. Hoster and X. W. D. Lou, *Energy Environ. Sci.*, 2014, **7**, 302–305.
134 J. S. Cho, Y. J. Hong and Y. C. Kang, *ACS Nano*, 2015, **9**, 4026–4035.
135 K. Fu, L. Xue, O. Yildiz, S. Li, H. Lee, Y. Li, G. Xu, L. Zhou, P. D. Bradford and X. Zhang, *Nano Energy*, 2013, **2**, 976–986.
136 X. Zhou, L. J. Wan and Y. G. Guo, *Small*, 2013, **9**, 2684–2688.

 This journal is © The Royal Society of Chemistry 2017

Published on 20 June 2017. Downloaded by University of Western Ontario on 27/07/2017 20:28:34.

137 J. Wang, Y. Yu, L. Gu, C. Wang, K. Tang and J. Maier, *Nanoscale*, 2013, **5**, 2647–2650.
138 X. Zhou, Z. Dai, S. Liu, J. Bao and Y. G. Guo, *Adv. Mater.*, 2014, **26**, 3943–3949.
139 L. Ji, O. Toprakci, M. Alcoutlabi, Y. Yao, Y. Li, S. Zhang, B. Guo, Z. Lin and X. Zhang, *ACS Appl. Mater. Interfaces*, 2012, **4**, 2672–2679.
140 M. Zhang, E. Uchaker, S. Hu, Q. Zhang, T. Wang, G. Cao and J. Li, *Nanoscale*, 2013, **5**, 12342–12349.
141 Z. Yang, G. Du, Q. Meng, Z. Guo, X. Yu, Z. Chen, T. Guo and R. Zeng, *J. Mater. Chem.*, 2012, **22**, 5848–5854.
142 Z. Yang, G. Du, Z. Guo, X. Yu, Z. Chen, T. Guo and H. Liu, *J. Mater. Chem.*, 2011, **21**, 8591–8596.
143 L. Xue, K. Fu, Y. Li, G. Xu, Y. Lu, S. Zhang, O. Toprakci and X. Zhang, *Nano Energy*, 2013, **2**, 361–367.
144 Y. Yu, L. Gu, C. Wang, A. Dhanabalan, P. A. van Aken and J. Maier, *Angew. Chem., Int. Ed.*, 2009, **48**, 6485–6489.
145 S. Abouali, M. A. Garakani, B. Zhang, H. Luo, Z.-L. Xu, J.-Q. Huang, J. Huang and J.-K. Kim, *J. Mater. Chem. A*, 2014, **2**, 16939–16944.
146 W.-H. Ryu, J. Shin, J.-W. Jung and I.-D. Kim, *J. Mater. Chem. A*, 2013, **1**, 3239–3243.
147 Z. Lu, N. Liu, H.-W. Lee, J. Zhao, W. Li, Y. Li and Y. Cui, *ACS Nano*, 2015, **9**, 2540–2547.
148 B. Zhang, J. Huang and J. K. Kim, *Adv. Funct. Mater.*, 2015, **25**, 5222–5228.
149 M.-H. Ryu, K.-N. Jung, K.-H. Shin, K.-S. Han and S. Yoon, *J. Phys. Chem. C*, 2013, **117**, 8092–8098.
150 L. Xia, S. Wang, G. Liu, L. Ding, D. Li, H. Wang and S. Qiao, *Small*, 2016, **12**, 853–859.
151 N. Zhu, W. Liu, M. Xue, Z. Xie, D. Zhao, M. Zhang, J. Chen and T. Cao, *Electrochim. Acta*, 2010, **55**, 5813–5818.
152 J. W. Fergus, *J. Power Sources*, 2010, **195**, 939–954.
153 M. S. Islam and C. A. Fisher, *Chem. Soc. Rev.*, 2014, **43**, 185–204.
154 L.-X. Yuan, Z.-H. Wang, W.-X. Zhang, X.-L. Hu, J.-T. Chen, Y.-H. Huang and J. B. Goodenough, *Energy Environ. Sci.*, 2011, **4**, 269–284.
155 C. Zhu, Y. Yu, L. Gu, K. Weichert and J. Maier, *Angew. Chem., Int. Ed.*, 2011, **50**, 6278–6282.
156 Q. Chen, X. Qiao, C. Peng, T. Zhang, Y. Wang and X. Wang, *Electrochim. Acta*, 2012, **78**, 40–48.
157 L. Dimesso, C. Spanheimer, W. Jaegermann, Y. Zhang and A. Yarin, *J. Appl. Phys.*, 2012, **111**, 064307.
158 O. Toprakci, H. A. Toprakci, L. Ji, G. Xu, Z. Lin and X. Zhang, *ACS Appl. Mater. Interfaces*, 2012, **4**, 1273–1280.
159 S. Zhang, Z. Lin, L. Ji, Y. Li, G. Xu, L. Xue, S. Li, Y. Lu, O. Toprakci and X. Zhang, *J. Mater. Chem.*, 2012, **22**, 14661–14666.
160 R. von Hagen, H. Lorrmann, K. C. Möller and S. Mathur, *Adv. Energy Mater.*, 2012, **2**, 553–559.
161 S. Zhang, Y. Li, G. Xu, S. Li, Y. Lu, O. Toprakci and X. Zhang, *J. Power Sources*, 2012, **213**, 10–15.
162 X. Fang, M. Ge, J. Rong and C. Zhou, *ACS Nano*, 2014, **8**, 4876–4882.
163 C. Zhu, Y. Wen, P. A. van Aken, J. Maier and Y. Yu, *Adv. Funct. Mater.*, 2015, **25**, 2335–2342.
164 J. Liu, Y. Wen, Y. Wang, P. A. van Aken, J. Maier and Y. Yu, *Adv. Mater.*, 2014, **26**, 6025–6030.
165 Y. Zhu, X. Fan, L. Suo, C. Luo, T. Gao and C. Wang, *ACS Nano*, 2015, **10**, 1529–1538.
166 P. Ge and M. Fouletier, *Solid State Ionics*, 1988, **28**, 1172–1175.
167 Y. Wen, K. He, Y. Zhu, F. Han, Y. Xu, I. Matsuda, Y. Ishii, J. Cumings and C. Wang, *Nat. Commun.*, 2014, **5**, 4033.
168 Y. Liu, B. V. Merinov and W. A. Goddard, *Proc. Natl. Acad. Sci. U. S. A.*, 2016, **113**, 3735–3739.
169 Y. Zhu, X. Han, Y. Xu, Y. Liu, S. Zheng, K. Xu, L. Hu and C. Wang, *ACS Nano*, 2013, **7**, 6378–6386.
170 S. Komaba, W. Murata, T. Ishikawa, N. Yabuuchi, T. Ozeki, T. Nakayama, A. Ogata, K. Gotoh and K. Fujiwara, *Adv. Funct. Mater.*, 2011, **21**, 3859–3867.
171 W. Luo, J. Schardt, C. Bommier, B. Wang, J. Razink, J. Simonsen and X. Ji, *J. Mater. Chem. A*, 2013, **1**, 10662–10666.
172 Z. Zhang, J. Zhang, X. Zhao and F. Yang, *Carbon*, 2015, **95**, 552–559.
173 T. Chen, Y. Liu, L. Pan, T. Lu, Y. Yao, Z. Sun, D. H. Chua and Q. Chen, *J. Mater. Chem. A*, 2014, **2**, 4117–4121.
174 S. Wang, L. Xia, L. Yu, L. Zhang, H. Wang and X. W. D. Lou, *Adv. Energy Mater.*, 2016, **6**, 1502217.
175 J. Jin, B.-j. Yu, Z.-q. Shi, C.-y. Wang and C.-b. Chong, *J. Power Sources*, 2014, **272**, 800–807.
176 L. Zeng, W. Li, J. Cheng, J. Wang, X. Liu and Y. Yu, *RSC Adv.*, 2014, **4**, 16920–16927.
177 J. Zhu, C. Chen, Y. Lu, Y. Ge, H. Jiang, K. Fu and X. Zhang, *Carbon*, 2015, **94**, 189–195.
178 C. Chen, Y. Lu, Y. Ge, J. Zhu, H. Jiang, Y. Li, Y. Hu and X. Zhang, *Energy Technol.*, 2016, **4**, 1440–1449.
179 M. Wang, Y. Yang, Z. Yang, L. Gu, Q. Chen and Y. Yu, *Adv. Sci.*, 2017, **4**, 1600468.
180 C.-Y. Chou, M. Lee and G. S. Hwang, *J. Phys. Chem. C*, 2015, **119**, 14843–14850.
181 M. Dirican, Y. Lu, Y. Ge, O. Yildiz and X. Zhang, *ACS Appl. Mater. Interfaces*, 2015, **7**, 18387–18396.
182 Y. Xu, Y. Zhu, Y. Liu and C. Wang, *Adv. Energy Mater.*, 2013, **3**, 128–133.
183 Y. Liu, N. Zhang, L. Jiao and J. Chen, *Adv. Mater.*, 2015, **27**, 6702–6707.
184 L. Ji, M. Gu, Y. Shao, X. Li, M. H. Engelhard, B. W. Arey, W. Wang, Z. Nie, J. Xiao and C. Wang, *Adv. Mater.*, 2014, **26**, 2901–2908.
185 K. Shiva, H. B. Rajendra and A. J. Bhattacharyya, *ChemPlusChem*, 2015, **80**, 516–521.
186 J. Liu, K. Tang, K. Song, P. A. van Aken, Y. Yu and J. Maier, *Phys. Chem. Chem. Phys.*, 2013, **15**, 20813–20818.
187 Y. Xiong, J. Qian, Y. Cao, X. Ai and H. Yang, *ACS Appl. Mater. Interfaces*, 2016, **8**, 16684–16689.
188 Y. Liu, N. Zhang, C. Yu, L. Jiao and J. Chen, *Nano Lett.*, 2016, **16**, 3321–3328.
189 X. Xiong, W. Luo, X. Hu, C. Chen, L. Qie, D. Hou and Y. Huang, *Sci. Rep.*, 2015, **5**, 9254.
190 J. S. Cho, S. Y. Lee and Y. C. Kang, *Sci. Rep.*, 2016, **6**, 23338.

Published on 20 June 2017. Downloaded by University of Western Ontario on 27/07/2017 20:28:34.

191 J. S. Cho, J.-K. Lee and Y. C. Kang, *Sci. Rep.*, 2016, **6**, 23699.
192 F. Sauvage, L. Laffont, J.-M. Tarascon and E. Baudrin, *Inorg. Chem.*, 2007, **46**, 3289–3294.
193 J. Tarascon, D. Guyomard, B. Wilkens, W. Mc Kinnon and P. Barboux, *Solid State Ionics*, 1992, **57**, 113–120.
194 R. Berthelot, D. Carlier and C. Delmas, *Nat. Mater.*, 2011, **10**, 74–80.
195 C. Zhu, K. Song, P. A. van Aken, J. Maier and Y. Yu, *Nano Lett.*, 2014, **14**, 2175–2180.
196 P. Moreau, D. Guyomard, J. Gaubicher and F. Boucher, *Chem. Mater.*, 2010, **22**, 4126–4128.
197 K. T. Lee, T. Ramesh, F. Nan, G. Botton and L. F. Nazar, *Chem. Mater.*, 2011, **23**, 3593–3600.
198 H. Li, Y. Bai, F. Wu, Y. Li and C. Wu, *J. Power Sources*, 2015, **273**, 784–792.
199 S. Kajiyama, J. Kikkawa, J. Hoshino, M. Okubo and E. Hosono, *Chem.–Eur. J.*, 2014, **20**, 12636–12640.

This journal is © The Royal Society of Chemistry 2017